INL/RPT-23-74540

Development of Surveillance Test Articles with Reduced Dimensions and Material Volumes to Support MSR Materials Degradation Management

September 2023

Heramb Mahajan, Xinchang Zhang, Kaelee Novich, Michael McMurtrey, Tate Patterson, Mahmut N. Cinbiz, and Ting-Leung Sham
Idaho National Laboratory

Idaho National Laboratory

INL is a U.S. Department of Energy National Laboratory operated by Battelle Energy Alliance, LLC

INL/RPT-23-74540

Development of Surveillance Test Articles with Reduced Dimensions and Material Volumes to Support MSR Materials Degradation Management

Heramb Mahajan, Xinchang Zhang, Kaelee Novich, Michael McMurtrey, Tate Patterson, Mahmut N. Cinbiz, and Ting-Leung Sham
Idaho National Laboratory

September 2023

Idaho National Laboratory
Advanced Reactor Technologies
Idaho Falls, Idaho 83415

http://www.art.inl.gov

Prepared for the
U.S. Department of Energy
Office of Nuclear Energy
Under DOE Idaho Operations Office
Contract DE-AC07-05ID14517

Page intentionally left blank

INL ART Program

Development of Surveillance Test Articles with Reduced Dimensions and Material Volumes to Support MSR Materials Degradation Management

INL/RPT-23-74540

September 2023

Technical Reviewer: (Confirmation of mathematical accuracy, and correctness of data and appropriateness of assumptions.)

ninadmohale — 8/29/2023

Ninad Mohale — Date
Materials Engineer

Approved by:

8/30/2023

Michael E. Davenport — Date
ART Project Manager

8/30/2023

Travis R. Mitchell — Date
ART Program Manager

8/29/2023

Michelle T. Sharp — Date
INL Quality Assurance

Page intentionally left blank

ABSTRACT

This report details the efforts toward developing new surveillance test article designs with reduced dimensions and material volumes to support materials surveillance technology development for advanced reactors. Two fabrication methods for the surveillance test articles are described. Welded test articles were fabricated with 316H and A617 materials, and interlocking test articles were fabricated using A709 and titanium-zirconium-molybdenum (TZM). The preliminary results demonstrate the successful design and testing of the flat surveillance test articles. The report also describes ongoing efforts to use an induction heating test setup to increase the heat up and cool down rates in testing the surveillance test articles. A brief description of the planned FY-24 work is provided.

Page intentionally left blank

ACKNOWLEDGEMENTS

This research was sponsored by the U.S. Department of Energy (DOE) under Contract No. DE-AC07-05ID14517 with Idaho National Laboratory (INL), which is managed and operated by Battelle Energy Alliance. Programmatic direction was provided by the Office of Nuclear Reactor Deployment of the DOE Office of Nuclear Energy (NE).

The authors gratefully acknowledge the support provided by Sue Lesica of DOE-NE, Federal Lead for Advanced Materials, Advanced Reactor Technologies (ART) Program; Janelle Eddins of DOE-NE, Federal Manager, ART Molten Salt Reactors (MSR) Campaign; and Patricia Paviet of Pacific Northwest National Laboratory, National Technical Director, ART MSR Campaign.

The authors also thank the assistance of David Cottle, Austin Matthews, and Joel Simpson of INL for experimental support.

Page intentionally left blank

CONTENTS

1. INTRODUCTION 1
2. WELDED CYLINDRICAL TEST ARTICLE 4
3. WELDED FLAT SURVEILLANCE TEST ARTICLE 5
3.1. Test Article Design and Fabrication 5
3.1.1. Design Approach 5
3.1.2. Design and Fabrication Evolution History 6
3.2. Experimental Setup 8
3.2.1. Furnace Heating Test Setup 8
3.2.2. Induction Heating Test Setup 9
3.3. Test Results 11
4. INTERLOCKING FLAT SURVEILLANCE TEST ARTICLE 17
4.1. Design Approach and Test Setup 18
4.2. Test Results 19
5. SUMMARY AND FUTURE WORK 20
6. REFERENCE 21
Appendix A Digital Image Correlation 23
A-1. DIC: Room Temperature Tension Test 24
A-2. DIC: Elevated Temperature Tension Test 27
A-3. DIC: Short Term Creep Test at Elevated Temperature 28

FIGURES

Figure 1. Different components of a typical surveillance test article assembly. 3
Figure 2. Induction heating test setup for cylindrical test article with right image showing test article at high temperature. 4
Figure 3. Schematic figures showing geometry and welds of (a) cylindrical surveillance test article and (b) flat surveillance test article. 6
Figure 4. Version 1 of the WFSTA design shows the dimensions and geometry with different materials and pre-weld test article assembly. 6
Figure 5. The welding gadget to support the WFSTA during welding and post-weld WFSTA version 1. 7
Figure 6. The solidification cracking observed in the WFSTA version 1 welding trials. 7
Figure 7. Version 2 of the WFSTA design showing the dimensions and geometry with different materials, pre-weld test article assembly, and welded test article. 8
Figure 8. Welded regions of the WFSTA version 2 showing no solidification cracking. 8

Figure 9. (a) Side view and (b) front view of the furnace heating setup with WFSTA in place. 9

Figure 10. (a) Thermocouple result showing interference due to induction heating setup, (b) thermocouple reader with a temperature input module that mitigated interference during temperature cycle. 9

Figure 11. Induction heating setup with spring type induction coil design and an image of a WFSTA version 1 at peak temperature. 10

Figure 12. Induction heating setup with observed temperature gradients (a) without the susceptor plate and (b) with the susceptor plate. 11

Figure 13. Temperature and DIC-strain on the WFSTA Sample 1 for the first 10 cycles and last 15 cycles, and the specimen after cooldown to room temperature with an arrow showing the out-of-plane deformation of driver-and-specimen assembly. 12

Figure 14. Strain time history of the total strain measured from DIC and the specimen after cooldown to room temperature, with a red arrow showing the out-of-plane deformation of the driver-specimen assembly. 13

Figure 15. Bent WFSTA Sample 1 with the image showing the out-of-plane deformation at one location between the A617 driver and 316H column. 13

Figure 16. Temperature history and stress-strain response from the FE analysis of the WFSTA showing the ramp-up, temperature cycles, and ramp-down phases of two load cases. 14

Figure 17. Comparison of the total strain history from FE simulations of a WFSTA against the strain history measured from the DIC on the WFSTA Sample 1 with strain ranges. 15

Figure 18. Temperature and DIC-strain on the WFSTA Sample 2 for 20 cycles, and the specimen after cooldown to room temperature with a red arrow showing the out-of-plane deformation of driver-and-specimen assembly. 16

Figure 19. Bent WFSTA Sample 2 with the image showing the out-of-plane deformation at one location between A617 driver and 316H column. 16

Figure 20. Test article geometry comparison with a given temperature cycle for specimen and column material of 316H shown in blue-colored and red-colored driver material A617 and TZM. 17

Figure 21. Interlocking test article assembly with TZM and A709. 18

Figure 22. Interlocking test article in glass assembly with argon gas environment. The furnace heating test setup was used to test this test article. 19

Figure 23. Evolution of DIC-strain during thermal cycling of an IFSTA. 20

Figure 24. Experimental setup for room-temperature tensile testing on flat tensile specimen. 24

Figure 25. End-of-test engineering strain on SS316L tensile specimen obtained by DIC analysis. 25

Figure 26. (a) Evolution of DIC strain and extensometer strain and (b) tensile stress-strain curves during tensile testing of SS316L at room temperature. 26

Figure 27. (a) Evolution of DIC strain and extensometer strain and (b) tensile stress-strain curves during tensile testing of Inconel 625 at room temperature. 26

Figure 28. (a) Experimental setup for elevated-temperature tensile testing of SS316L in a ATS creep frame, (b) dimensions of tensile specimen, and (c) manual loading procedures. 27

Figure 29. (a) End-of-test strain and (b) strain history obtained by LVDT and DIC in tensile testing of SS316L at 700°C. 28
Figure 30. (a) Experimental setup for creep testing of a SS316H specimen at 875°C and 30 MPa, (b) evolution of strain obtained by LVDT and DIC. 29

Page intentionally left blank

ACRONYMS

ANL	Argonne National Laboratory
ART	Advanced Reactor Technologies
ASME	American Society of Mechanical Engineers
ASTM	American Society for Testing and Materials
ATS	Applied Test Systems
CTE	Coefficient of thermal expansion
DIC	Digital image correlation
DOE	(U.S.) Department of Energy
FE	Finite element
FIB	Focused ion beam
HBB	Subsection HB, Subpart B
INL	Idaho National Laboratory
ISG	Interim staff guidance
IFSTA	Interlocking flat surveillance test article
LWR	Light water reactor
LVDT	Linear variable differential transformer
MSR	Molten salt reactor
NE	Nuclear energy
NRC	Nuclear Regulatory Commission
RIM	Reliability and integrity management
RV	Reactor vessel
SMT	Simplified model test
SS	Stainless steel
TZM	Titanium-zirconium-molybdenum
WFSTA	Welded flat surveillance test article

Page intentionally left blank

Development of Surveillance Test Articles with Reduced Dimensions and Material Volumes to Support MSR Materials Degradation Management

1. INTRODUCTION

Molten salt reactors (MSR) operate in the elevated temperature range of 600–750°C. Some MSR designs have nuclear fuel dissolved in the molten salt, which is circulated within the reactor primary loop and subjects the coolant boundary components to materials degradation due to thermal cycling, corrosion, and radiation damage during MSR operations.

The operating experience of MSRs is less than other advanced reactor systems such as gas-cooled reactors and sodium fast reactors. Information is limited on materials degradations due to irradiation, corrosion, elevated temperature exposure and stress during MSR operations. Establishing a materials surveillance program that allows information collection on these materials degradations could be an important pathway to support the timely licensing of MSRs.

The American Society of Mechanical Engineers (ASME) Boiler and Pressure Vessel Code, Section III, Division 5 [1] provides the construction rules for structural components of high-temperature reactors. Section III, Division 5, Subsection HB, Subpart B (HBB) specifies the mechanical properties and allowable stresses to be used for designing metallic components at elevated temperature under cyclic service. The scope of HBB states that the rules do not provide methods to evaluate deterioration that may occur in service due to corrosion, mass transfer phenomena, radiation effects, or other material instabilities. These effects shall be considered to understand the design or the specified life of the components and supports. Changes in material properties subjected to neutron radiation may be checked periodically by means of material surveillance programs.

The need for performance monitoring and surveillance programs, particularly for long design lifetimes (i.e., 500,000 hours), has been reinforced in HBB recently. A general note has been added to HBB, which emphasizes that the time-dependent allowable stresses are extrapolated from shorter term test data using an engineering model. For longer design lives, the designer should consider further strength reductions to account for potential in-service material degradation. Additionally, enhanced material surveillance programs and heightened in-service inspection per the rules of ASME Section XI, Division 2 [2] may be warranted.

The U.S. Nuclear Regulatory Commission (NRC) has recently issued a Draft Interim Staff Guidance (ISG) on Material Compatibility for advanced non-light water reactors (LWRs) [3]. The ISG identifies information related to materials qualification the NRC staff should consider in the license review. It also indicates where it may be appropriate to rely on monitoring and surveillance to provide reasonable assurance of structural integrity.

The current materials surveillance program for LWRs was developed to address integrity assessments of reactor vessel (RV). ASME Section III, Division 1, Subsection NB [4] has provisions for properties in the unirradiated condition. Changes in properties due to irradiation are monitored using the surveillance program. The primary material property of interest for RV integrity of LWRs is the fracture toughness of the RV material. Charpy-V notch impact specimen for the base and weld metals are irradiated in surveillance capsules. The surveillance programs for LWRs are designed to examine the status of RV material properties and to predict the changes in these properties resulting from the cumulative effects of radiation.

The American Society for Testing and Materials (ASTM) E531, "Standard Practice for Surveillance Testing of High-Temperature Nuclear Component Materials" [5], was initially published in 1975, based on the surveillance technology for LWRs. The ASTM committee recently reevaluated E531 and concluded that the standard practice needs to be revised to render the practice to be useful for the current advanced reactor designs that are being considered by the industry. E531 was withdrawn in 2022, and revision is ongoing.

The establishment of a materials surveillance program for advanced reactors is challenging as the surveillance test article needs to capture the effects of neutron irradiation, salt corrosion, temperature, and stress. To actively apply creep-fatigue loading on the surrogate material in a surveillance test article is very difficult as the use of cables and bellows to apply the loads in an operating advanced reactor is not practical.

With the understanding of structural interactions in a simplified model test (SMT) specimen [6] developed by the DOE-NE Advanced Reactors Technologies (ART) program, Idaho National Laboratory (INL) and Argonne National Laboratory (ANL) have developed a viable concept for the surveillance test article in which the surrogate material can be subject to prototypical cyclic strain ranges during thermal transients under the ART MSR Campaign. The thermal cycling of the surrogate material is driven by the thermal expansion mismatch of the materials used to construct the surveillance test article. Mechanical interaction effects, such as stress relaxation, have been considered when establishing the design envelope for the surveillance test articles.

There are many challenges in developing surveillance test articles for advanced reactor applications. One challenge is to reduce the sizes and, thus, the material volumes of the surveillance test articles to reduce the restrictions on their placement locations within the reactor and the volume of activated materials from reactor operations. Reducing these would allow for the possibility of test articles retrieval; out-of-pile testing, such as thermal cycling or instrumented indentation testing; and re-insertion of the test articles for additional materials surveillance for continued reactor operation.

The reduced surveillance test article sizes introduce challenges in test article fabrication, in testing, and collection of validation data.

The past work on the surveillance test article development is outlined below.

ANL development effort (details are documented in References [7, 8, 9]):

1. The initial development of passively loaded test article design was conducted by ANL, and it involved the use of the coefficient of thermal expansion (CTE) mismatch of two materials. After reviewing the characteristics of the structural responses of reactor components, two critical mechanical parameters were identified that would characterize the structural response: strain range and elastic follow-up. The surveillance test article design uses these two parameters in the test article design process. As the reactor experiences temperature transients, the CTE mismatch of two materials induces creep-fatigue cycling in the surveillance test article. A typical surveillance test article consists of an assembly of specimen, driver, and column/casing, as shown in Figure 1. The specimen is the material under investigation, the driver is the material with lower CTE value compared to specimen and column/casing, and the column/casing facilitate the expansion required to apply load.
2. The surveillance test article can be modeled structurally with a three-bar problem, which facilitated a test article design for a given strain range and elastic follow up. A test article was designed with a total length of 300 mm. The test article fabrication involved welding specimen, driver, and casing. Driver material was A617, and specimen and casing material were SS316H. Strain gauges were attached on the specimen. Cyclic temperature was applied to the test article. The concept of passive creep-fatigue loading was established from the results.

3. The proof-of-concept level test article was very large in size, so efforts were made to design smaller test articles with 75 mm long cylindrical samples. The test specimen and casing material was SS316H, and the driver material was A617 (nickel alloy). Test specimen, driver, and casing were welded using different techniques. Preliminary results showed success in the smaller test article fabrication. Although efforts were made to weld titanium-zirconium-molybdenum (TZM)-driver material to 316H, severe oxidation and cracking were observed near welds, even in an inert gas environment. Hence, welding was deemed as an infeasible option for the surveillance test article design with the TZM driver.

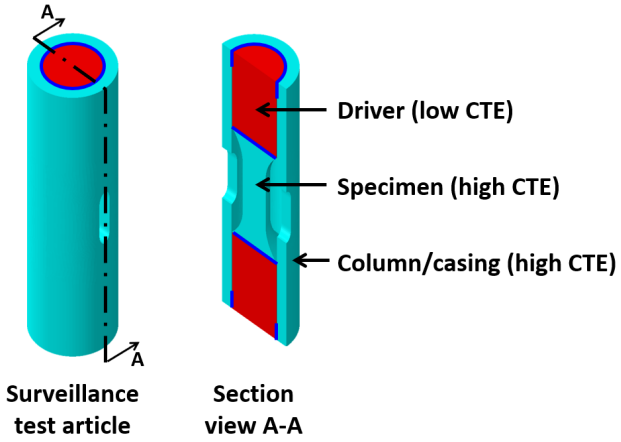

Figure 1. Different components of a typical surveillance test article assembly.

For all the tests discussed above, cyclic temperature profiles were applied to the test article using furnace heating. This test approach takes time as the heating and cooling rate of furnace is limited. INL explored the induction heating technique [10] in FY-22 to accelerate the test time as induction heating can apply at faster temperature cycles. There were some issues with the induction heating approach such as severe spatial temperature gradients along specimen dimensions.

Current challenges in the design, fabrication, and testing of the surveillance test articles and their deployment in operating reactors are listed below:

1. Welding may not be feasible – As discussed, a welding option may not be possible for all materials. Oxidation and cracking near welds could also become a weak point in the test article assembly, affecting the key surveillance parameters.
2. Fluid flow interruption – The smallest ANL test article is 75 mm long and has a 25 mm diameter cylindrical geometry. Although this test article is smaller compared to the proof-of-concept level, which is a 300 mm-long test article design, for some applications this test article size could be too large, resulting in the disruption of the coolant flow.
3. Large irradiation volume – Reducing sample size results in faster sample cooling, which makes quick life assessment and specimen handling an easy task.
4. Larger specimen size – The ANL surveillance test article design with 25 mm diameter and 75 mm length cannot be placed within certain reactor components such as small diameter pipes. These components require smaller test article design.

This report presents the work conducted in FY-23, which includes the new test article design with reduced dimensions, fabrication, and test results. The test results for welded test article show promise in capturing the strain range and elastic follow up.

This report also presents a new interlocking test article design, which overcomes the challenges of the welded test article design and facilitates the possible use of refractory alloys as the driver material. This will enhance the structural robustness of the surveillance test article due to their increased radiation and corrosion resistance and lower CTE. Issues with the induction heating techniques were resolved and presented in this report.

2. WELDED CYLINDRICAL TEST ARTICLE

The cylindrical test article design was originally developed at ANL [7]. This test article was fabricated in two steps. The first step was stir-friction welding a 316H rod to two pieces of A617 driver bars. A reduced section was machined in the 316H rod. This assembly was placed in the 316H casing and welded through electron beam welds. The detailed approach is described in Messner, et al. (2020), Messner, et al. (2021), and Messner, Momozaki, and Boron (2022) [7, 8, 9]. The cylindrical test article fabricated by ANL was used at INL with induction heating setup to accelerate the test time. The induction heating setup with apparatus and heated specimen is shown in Figure 2. The test article was placed on a fire resistant and thermally insulating ceramic brick.

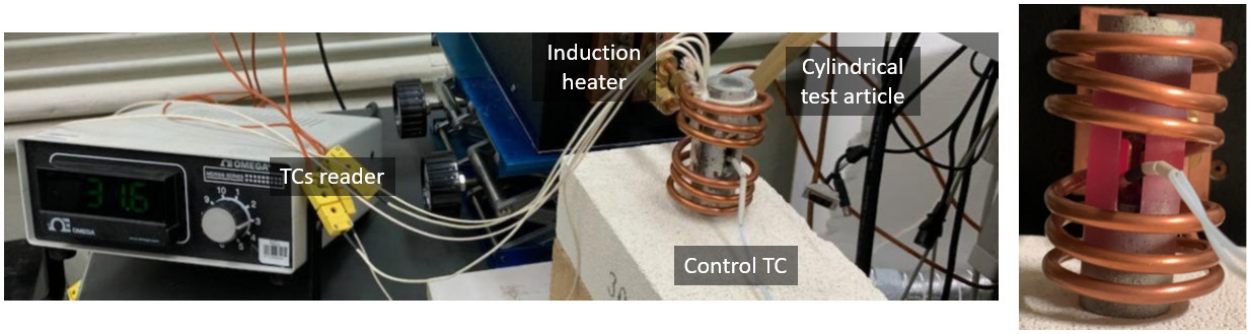

Figure 2. Induction heating test setup for cylindrical test article with right image showing test article at high temperature.

The first round of the induction heating test yielded a larger temperature gradient along the length of the casing. Higher temperature values were observed at the center compared to both ends. The specimen inside the casing was consistently at lower temperatures compared to the mid-length casing temperature. This temperature distribution is undesirable as the coefficient of the thermal mismatch approach works when the test article temperature, at any given time, is reasonably at same temperature. In case of temperature gradient along the casing length, the observed strain range and elastic follow-up values from the specimen will not reach the intended design values.

A series of optimization steps with modified coil designs was conducted to improve the thermal profile within the test article and a better temperature profile was achieved along the column length. However, the specimen inside the casing was significantly cooler compared to the casing temperature. When magnetic flux from the induction coil penetrates through the outer casing, the magnetic flux loses power, generating eddy currents in the casing, which results in increased casing temperature. Hence, the specimen inside the casing could not be heated with the same temperature amplitude as the casing. Based on this observation, it was decided that the induction heating setup is not the best suited for the cylindrical test article geometry. The furnace heating provides a more uniform temperature with lower temperature rates, making it the best option for the cylindrical test article design. A tube furnace with a maximum operating temperature of 1000°C was identified and recently updated to support the thermal cycling test of the ANL test article, which will occur in FY-24.

3. WELDED FLAT SURVEILLANCE TEST ARTICLE

3.1. Test Article Design and Fabrication

3.1.1. Design Approach

Initial work on the design and analysis of the surveillance test article by ANL [7, 8] has established the simplified analysis framework, which captures the key test article characteristics through defining a three-bar problem. This simplified analysis approach neglects effects due to notch and smooth corner and considers uniform cross-sectional bars. This approach reasonably and quickly provides estimated dimensions of test specimen. The test specimen geometry is optimized through a genetic algorithm optimization scheme available in the Python optimization library. A set of optimization constraints ensures the optimum geometry does not have any non-physical dimensions. The detailed analysis, optimization, and design approaches are discussed in the previous ANL work [7].

With the optimum dimensions for the ANL cylindrical test article, a detailed finite-element model with a viscoplastic constitutive model was carried out by INL in FY-22 [10] to simulate the test article response.

The design and analysis approach listed below is used:

1. Select strain range and elastic follow up: A critical location of a component will dictate these parameters. However, for the test article development work, reasonable parameter values were selected, which would allow for test article failure in a reasonable timeframe.
2. Optimize test article geometry: A constrained optimization technique with built-in genetic algorithms in the Python optimization library was employed to optimize the test article geometric parameters for the selected strain range and elastic follow up. This step provides the area ratios for test specimen, driver, and column/casing.
3. Detailed analysis: Optimized test article geometry from step 2 is used as input for a finite-element model with detailed geometry. Welds are simulated through gluing nodes from two different bodies implicitly suggesting perfect welds. A viscoplastic constitutive model used SS316 material, simplified inelastic model used A617, and elastic material properties used TZM-captured material response. Test article geometry is modified to minimize stresses at welds, if necessary.

The ANL cylindrical test article design can be scaled down to minimize the test article volume; however, the casing thickness of a scaled-down design is very small, resulting in fabrication challenges. Also, welding thin cylindrical casing to the very small driver rod is not practical.

Therefore, in FY-23, INL adopted a plate-like test article geometry, which simplifies the fabrication and the corresponding welding steps. Figure 3 compares the schematic representation of cylindrical and flat surveillance test article geometry. Alloy plates were procured, and desired geometry was machined through a wire electro-discharge machining (wire-EDM) technique. Welding techniques, such as electron-beam or laser beam, can easily penetrate thin plates of 1 mm thickness of material, ensuring good welds across thickness. For a cylindrical test article, the weld beam is along the specimen axis making it difficult to control of weld depth. For the flat test article, the weld beam is perpendicular to the test article plane, which provides adequate control for weld lengths. Weld quality inspection is easier and quicker for flat test article due to the weld accessibility. The fabrication and welding flexibility allow miniaturization of test specimen, overcoming the previously noted limitations of a large test article size. For given design parameters, the test article volume could be reduced by order of magnitude. These benefits make the flat test article a good candidate to reduce specimen dimensions. The design approach was identical to the cylindrical design approach, except areas of three-bar problem were associated with the rectangular area. The following subsections of Section 3 discuss the design, fabrication, and testing of a welded flat surveillance test article (WFSTA).

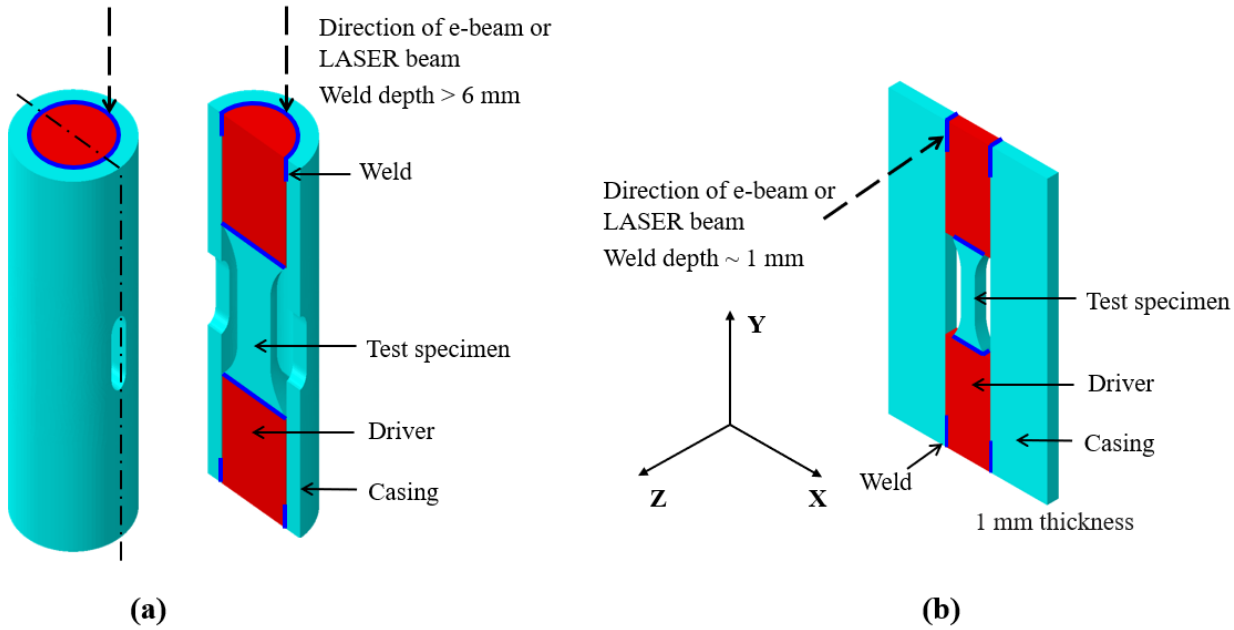

Figure 3. Schematic figures showing geometry and welds of (a) cylindrical surveillance test article and (b) flat surveillance test article.

3.1.2. Design and Fabrication Evolution History

Using the design approach discussed in the previous section resulted in the first iteration of a WFSTA design, as shown in Figure 4. The red lines show the intended weld length in the design, and the green lines show the gaps between the drivers, columns, and specimen. The left image in Figure 5 shows the specimen support gadget used during the welding process, and the right image shows the post-weld picture of a WFSTA. This design used minimum weld lengths required for load transfer between two materials. The welding parameters were optimized using this specimen design. Some of the initial welds entailed laser welding and an electron-beam welding approach. Figure 6 shows solidification cracking, which is highlighted by an arrow near welds at different locations and through different techniques. When the temperature cycle was applied to this test article, premature failure was noted near the weld lines originating from these solidification cracks between specimen and driver.

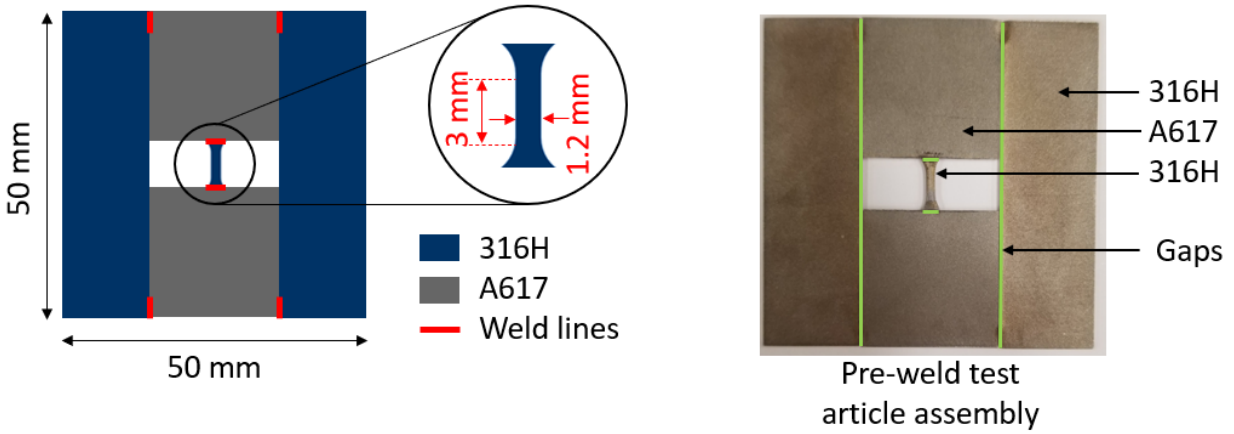

Figure 4. Version 1 of the WFSTA design shows the dimensions and geometry with different materials and pre-weld test article assembly.

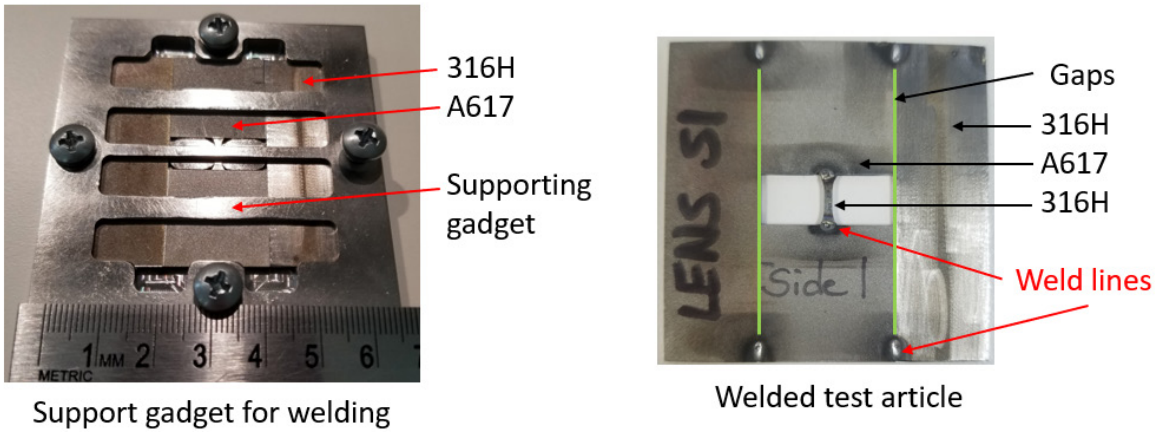

Figure 5. The welding gadget to support the WFSTA during welding and post-weld WFSTA version 1.

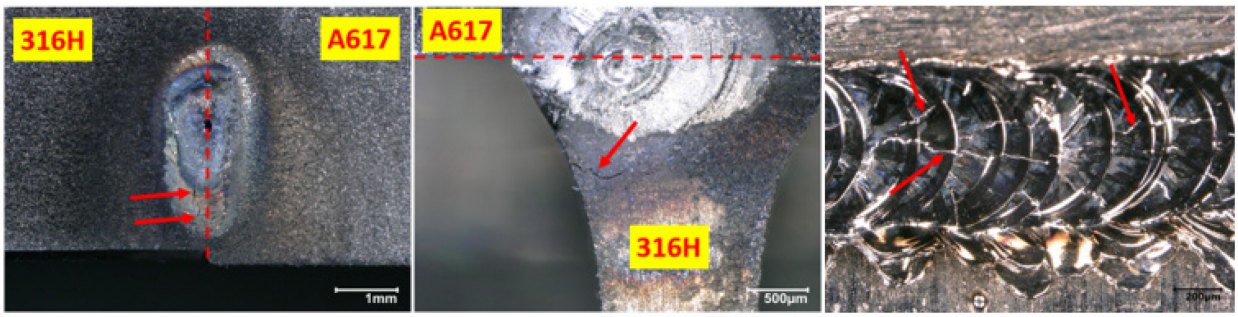

Figure 6. The solidification cracking observed in the WFSTA version 1 welding trials.

The second iteration of the WFSTA design, as shown in Figure 7, addressed these issues. The primary change in the new design was to increase the weld area to minimize weld stresses and minimize the influence of welds on stresses in the reduced section of specimen. Weld line orientation between columns and the driver were changed to minimize weld shear stress. Improved weld parameters successfully welded the test article. There were no visible solidification cracks on the version 2 test article, as shown in Figure 8. Optimum weld parameters used in the fabrication of the version 2 test article are listed below:

- No filler material
- Pulsed laser spot welding with approximately 70% spot overlap
- 1000 W of peak laser power with an approximately 100 μm beam diameter
- The power was linearly ramped up and down to mitigate solidification cracking
- Circular beam oscillation with an amplitude (diameter) of 0.5 mm was used to mitigate solidification cracking.

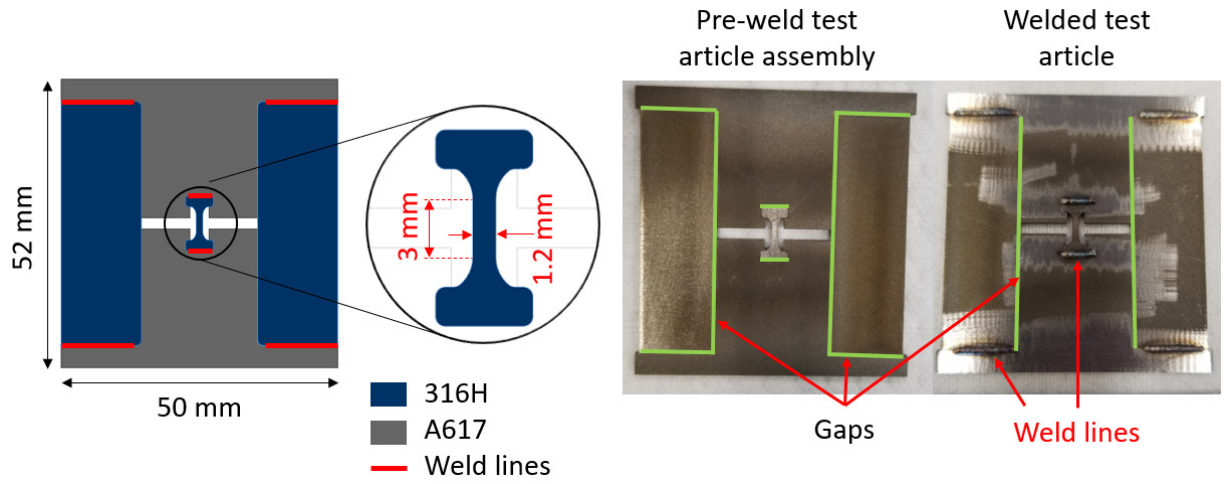

Figure 7. Version 2 of the WFSTA design showing the dimensions and geometry with different materials, pre-weld test article assembly, and welded test article.

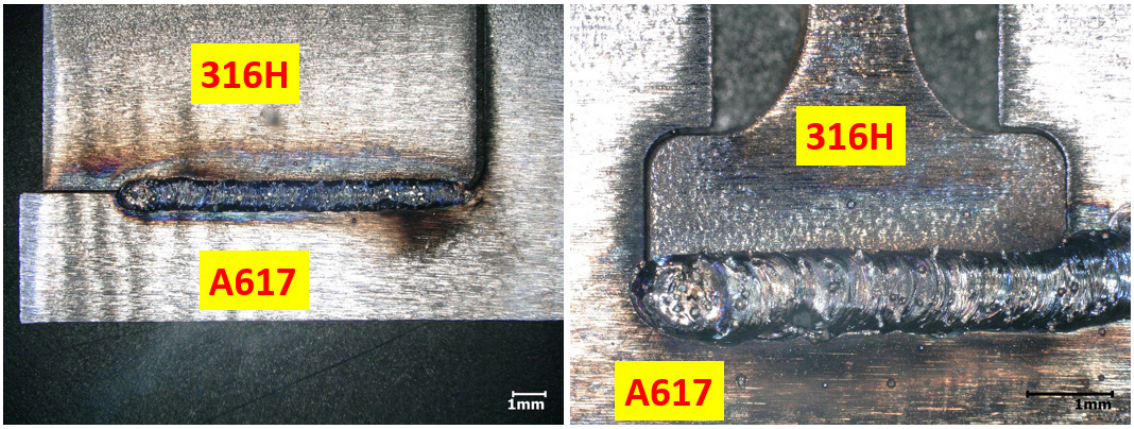

Figure 8. Welded regions of the WFSTA version 2 showing no solidification cracking.

3.2. Experimental Setup

3.2.1. Furnace Heating Test Setup

The furnace heating test setup involves tube furnace to apply temperature cycles and measure specimen strain with the digital image correlation (DIC) technique. To test the image qualities at high temperatures using the tube furnace heating method, a SS 316L specimen was used and heated up to 700°C. The test setup is shown in Figure 9. A type K thermocouple was attached to the specimen to measure the sample temperature as a calibration of the tube furnace. Figure 9 exhibits the temperature history measured by the thermocouple, which demonstrated a good match with the thermocouple reading of furnace. The DIC images were taken during the thermal expansion of the SS316L. At higher temperatures, heat haze introduced distortion in recorded images. These large distortions affect the recorded speckle pattern distribution and subsequent strain measurement, introducing a larger error in the DIC results. The tube furnace has an open camera viewport, which results in the convection of hot air with cooler ambient air giving a heat haze. The effect of this heat haze is amplified due to a long focal-length telescopic lens. To mitigate this issue, a fused silica glass window was designed, fabricated, and placed at the end of the tube furnace to prevent air convection at the camera viewport. Second, a desk

fan was used to mix the air around the optical path to even out the index of refraction. These two steps have successfully mitigated the haze waves on the DIC images.

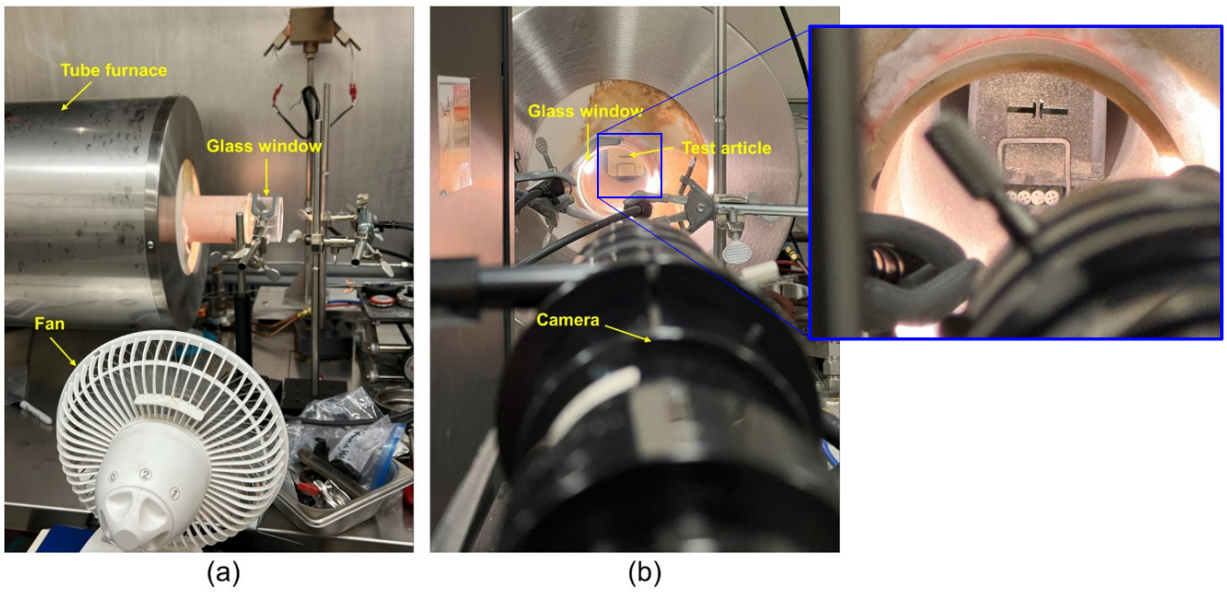

Figure 9. (a) Side view and (b) front view of the furnace heating setup with WFSTA in place.

3.2.2. Induction Heating Test Setup

One limitation of the furnace heating setup is the time required for temperature ramp up and cooldown. To test the surveillance test article in the laboratory, limited temperature ramp rates result in a very long test time for each test specimen. The induction heating technique overcomes this limitation by providing fast heat-up and cooldown rates. It uses electromagnetic fields to generate eddy currents in substrate. The substrate resistance to the induced eddy currents raises the substrate temperature. Previous induction heating work at INL showed electromagnetic fields from the induction coil interfere with thermocouples. This interference gives an unrealistic temperature reading, as shown by recorded thermocouple data in Figure 10a. This interference is mitigated through a National Instruments 9211, C-series temperature input module. This module has built-in anti-aliasing filters and noise immunity, providing a smoother thermocouple reading during induction heating, as shown in Figure 10b.

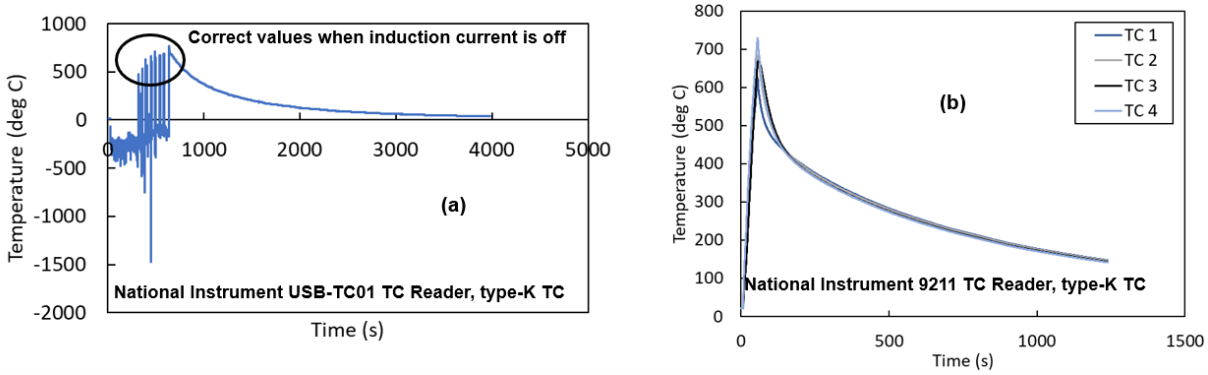

Figure 10. (a) Thermocouple result showing interference due to induction heating setup, (b) thermocouple reader with a temperature input module that mitigated interference during temperature cycle.

A controlling thermocouple with a closed loop to an Ambrell Model 5 (5kW) induction heater and associated Ameritherm chiller is used for cooling the induction heating coil and power supply. The National Instruments LabVIEW platform controls the heater and data acquisition system. The induction coil is designed for a WFSTA with specimen in a standing position, as shown in the Figure 11. A controlling thermocouple was attached to the specimen, and induction heating was raised specimen temperature. A larger spatial temperature gradient (about >100°C) was observed in a test article. This large temperature gradient is not desirable as it may result unintentional bending of columns or driver material and put excessive stresses on the welds. This temperature gradient will adversely affect intended strain ranges and elastic follow-up values.

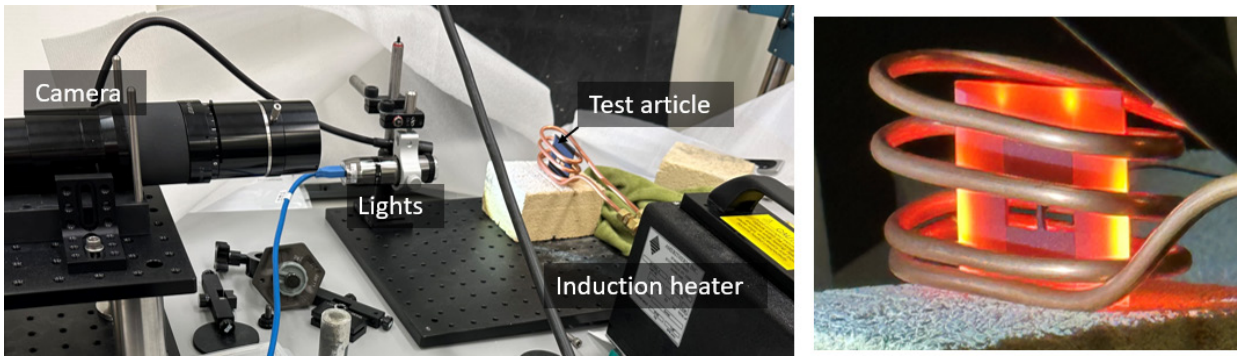

Figure 11. Induction heating setup with spring type induction coil design and an image of a WFSTA version 1 at peak temperature.

A new coil design was adopted with a concentric spiral geometry. The test article was sandwiched between quartz glass. The quartz glass was then placed on top of the coil, as shown in Figure 12a. Upon heating this setup, severe temperature gradients were observed along the width and length of the specimen. To minimize these temperature gradients, a susceptor plate was introduced between the quartz glass and a test article, as shown in Figure 12b. This susceptor plate provides more uniform heat to the test article. The temperature profile with the susceptor plate showed better temperature profile. The induction heater with a concentric induction coil design with susceptor plate was adopted. The special location of the sample near induction heater was critical to achieve a uniform temperature profile. Thus, a specimen holder gadget was designed and is undergoing the fabrication process to hold the specimen with a specific spatial orientation to produce repeatable and reliable temperature profiles for all test articles.

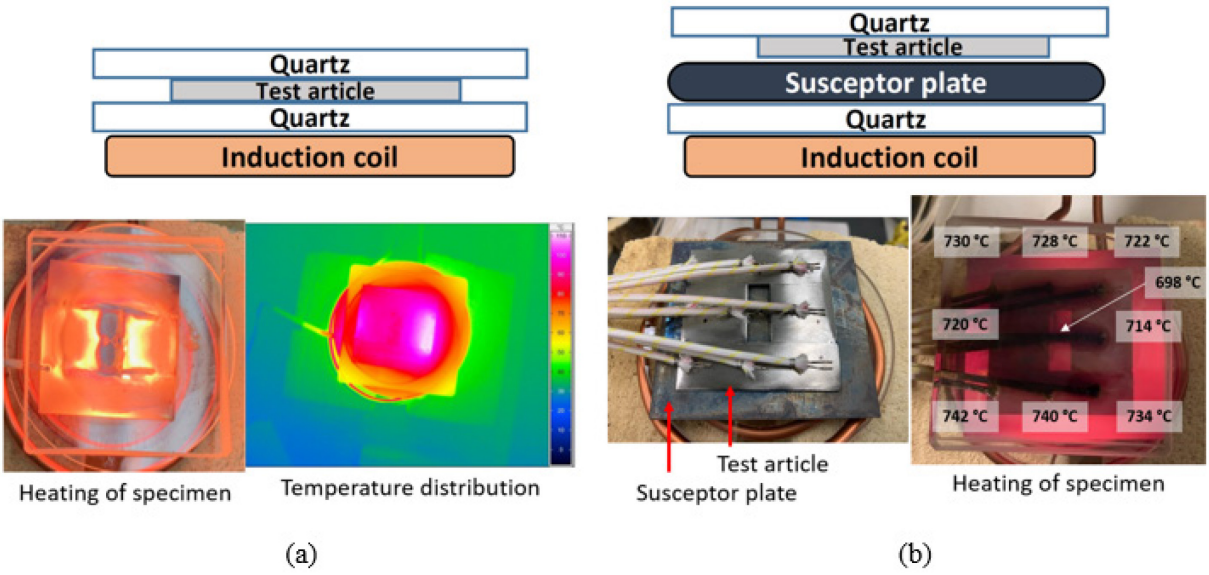

Figure 12. Induction heating setup with observed temperature gradients (a) without the susceptor plate and (b) with the susceptor plate.

3.3. Test Results

The spray-painted speckle pattern was applied on the WFSTA Sample 1. A total of 42 thermal cycles were applied on the test article from 500–700°C with a heating rate of 6°C/min and cooling rate of 2°C/min. The DIC strain data and temperature history from the first 10 and last 15 cycles is shown in Figure 13. The picture of the DIC speckle pattern at room temperature is taken as a reference image to set zero strain. The DIC speckle pattern yielded a poorer signal-to-noise ratio in the measured strain values. The calculated mechanical strain range from total strain range history was not feasible due to the large noise. Upon cooling, the specimen experienced a large compressive stress, which resulted in a slightly out-of-plane deformation of driver-specimen assembly, as shown in the Figure 13.

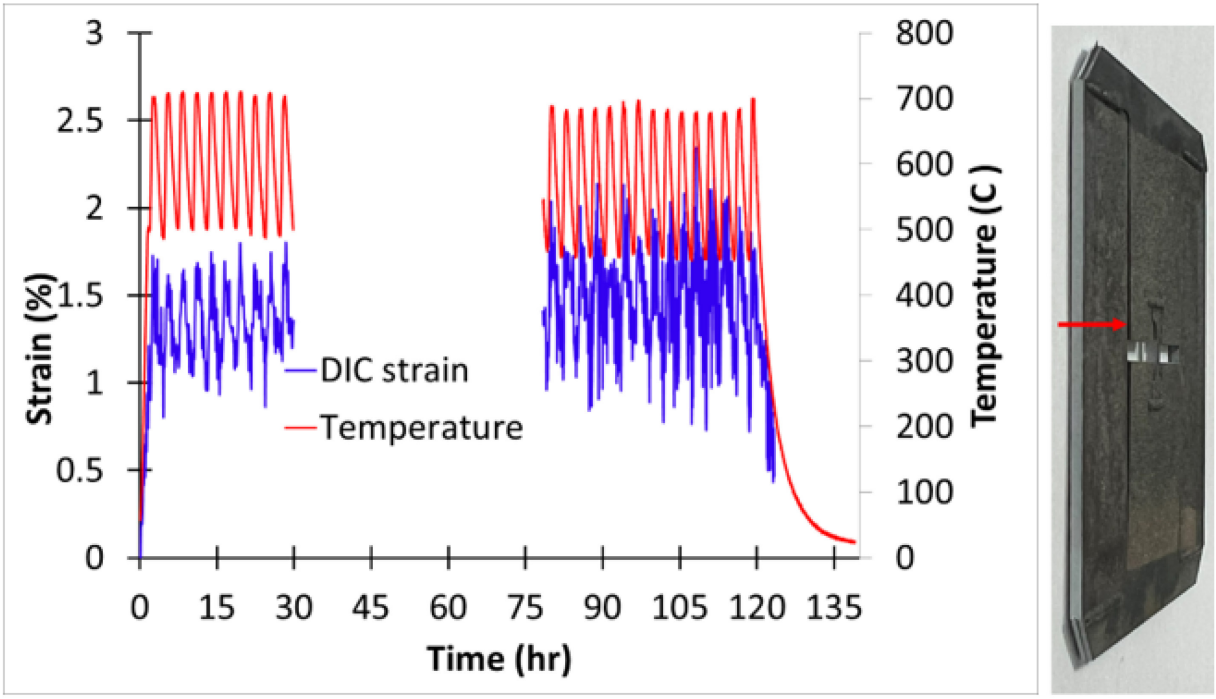

Figure 13. Temperature and DIC-strain on the WFSTA Sample 1 for the first 10 cycles and last 15 cycles, and the specimen after cooldown to room temperature with an arrow showing the out-of-plane deformation of driver-and-specimen assembly.

An extensive evaluation was conducted to validate and improve the quality of the strain data measured from the DIC technique. This extensive validation involved improving the speckle pattern, minimizing noise through removing heat haze, and a series of tests, including a room temperature tension test, an elevated temperature tension test, and a short-term pure creep test. A good agreement was observed between strain data measured from the DIC and strain from linear variable differential transformers (LVDTs) or extensometer. It was shown that a speckle pattern through airbrush achieved the best results. The detailed information regarding the test setup, specimen geometry, speckle pattern, and plots of DIC strain measurements are presented in Appendix A, "Digital Image Correlation."

The WFSTA Sample 1 was repainted with an airbrush and was re-loaded with 10 additional thermal cycles. Figure 14 shows in red and blue color the temperature and DIC-calculated strain history on a used WFSTA, respectively. The DIC image at the beginning of the experiment (~40°C) was used as the reference frame, where the strain was set to zero. Ratcheting was observed with the total strain range of 0.72% in the test article. Upon cooling to room temperature, bending was observed with larger out-of-plane deformation compared to the previous cooldown. This test demonstrated the successful tracking of strain evolution during furnace heating. No visible cracking was observed near welds. This test also shows the following:

- The test article can withstand multiple ramp-up, steady operation, and ramp-down cycles typical of advanced reactor operations.
- Strain ranges in specimen could be achieved even after a slight out-of-plane deflection (Figure 14).
- The test article could be removed from the reactor, assessed for accumulated damage, and placed back inside the reactor for continued damage accumulation.

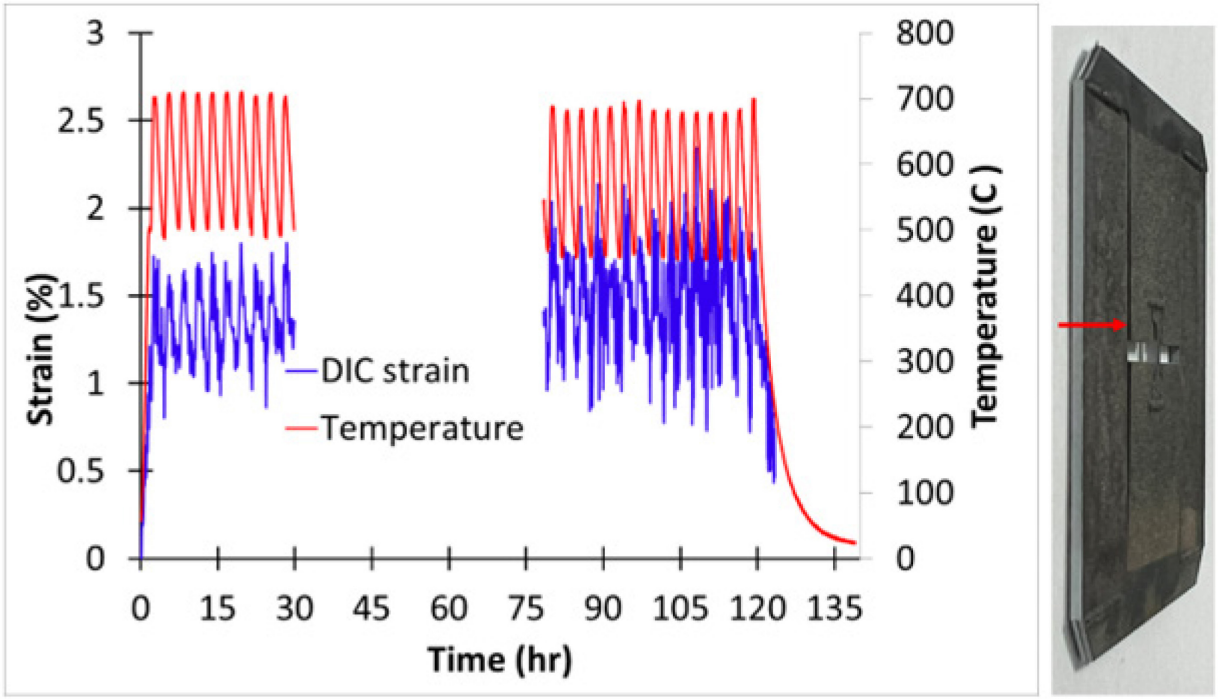

Figure 14. Strain time history of the total strain measured from DIC and the specimen after cooldown to room temperature, with a red arrow showing the out-of-plane deformation of the driver-specimen assembly.

The out-of-plane deformation is measured through the microscope, and the topographical image is shown in Figure 15. The out-of-plane deformation was measured at four locations, and one of the locations is highlighted in Figure 15. This location has the A617 driver deformed out-of-plane compared to 316H column. The average out-of-plane deformation from these columns was measured as 0.381mm. This deformation is caused by compressive stress during the ramp-down.

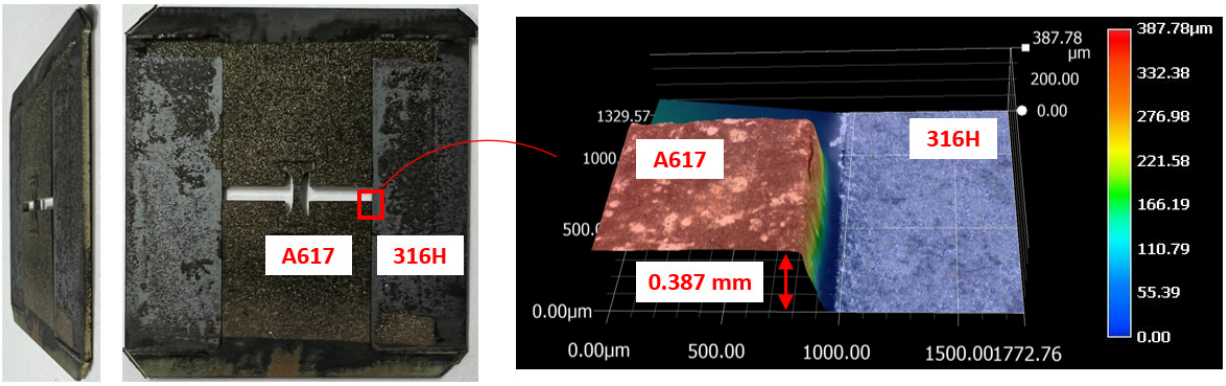

Figure 15. Bent WFSTA Sample 1 with the image showing the out-of-plane deformation at one location between the A617 driver and 316H column.

The applied temperature history and stress-strain response from the finite element (FE) simulation results of the specimen in a WFSTA is shown in Figure 16. The line color represents the respective temperature. The temperature "Ramp up 1" results in a strain ramp on the specimen, as shown in the stress-strain history response. During the temperature cycles from 500–700°C, the stress-strain response shows hysteresis loops going from tension to compression. The temperature "Ramp down 1" loads the specimen with a significant compressive stress. This is expected as larger, unloading strain is applied on the specimen, and the load carrying capacity of material increases as temperature cools down. This compressive stress results in an out-of-plane deformation. (Note that this deformation mode acts like a global buckling mode involving driver-specimen-driver assembly.) This minimizes the accumulated strain on the specimen. Upon the next temperature ramp-up cycle, the stress-strain state observed in the first ramp is achieved.

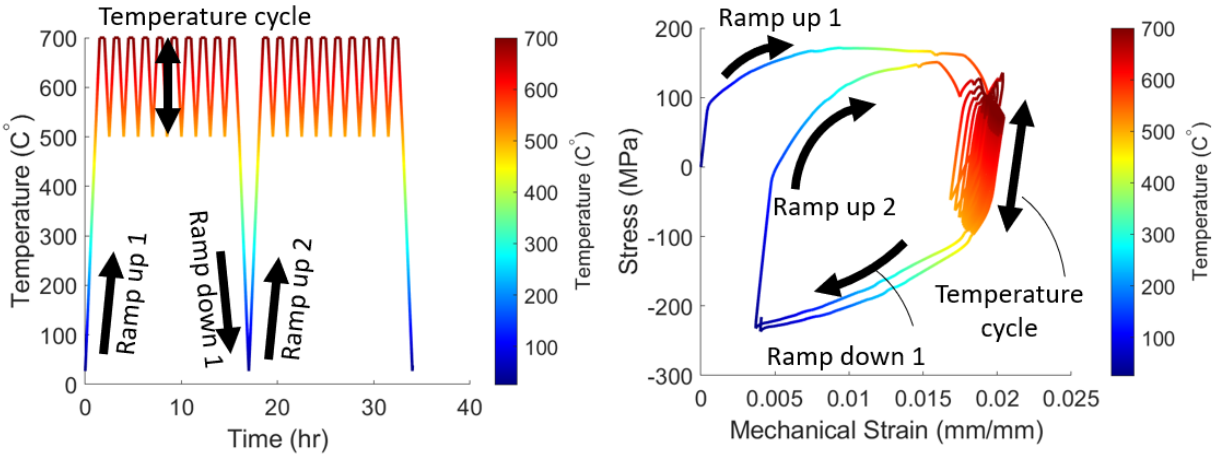

Figure 16. Temperature history and stress-strain response from the FE analysis of the WFSTA showing the ramp-up, temperature cycles, and ramp-down phases of two load cases.

The total strain response from FE simulations is compared against the DIC total strain from the test, as shown in Figure 17. Actual strain values are not a perfect match. The welding process may introduce localized residual stresses resulting in a non-zero stress state at the beginning of the test. Removing these residual stresses is not possible as any heating of a WFSTA would result in more stress accumulation due to a CTE mismatch between driver-specimen-driver assembly and columns. However, a reasonable comparison was observed between the simulated strain range and observed strain range in the test, showing the adopted analysis and design methodology yield an adequate estimation of the actual strain range observed in the specimen of the flat test article design.

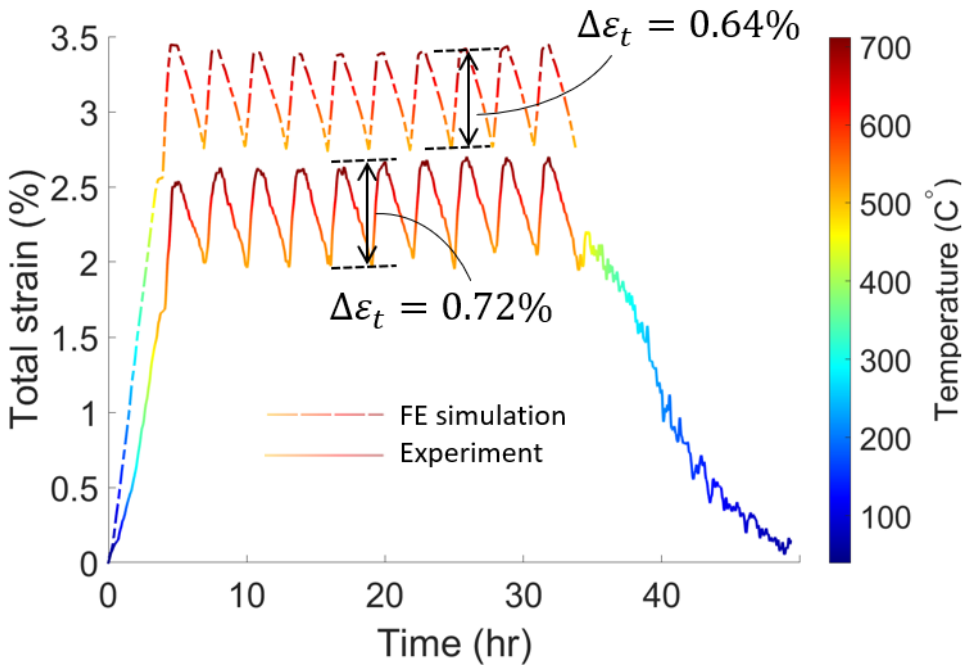

Figure 17. Comparison of the total strain history from FE simulations of a WFSTA against the strain history measured from the DIC on the WFSTA Sample 1 with strain ranges.

The WFSTA Sample 2 was painted with an airbrush and subjected to 20 temperature cycles. The temperature and DIC strain history is shown in Figure 18. The image at the 500℃ is taken as the reference image, meaning the strain is set at zero at 500℃. Upon cooling the WFSTA Sample 2 to room temperature, out-of-plane deformation was observed—similar to Sample 1. An average of 0.304 mm out-of-plane deformation was measured from four locations. Figure 19 shows one of the locations and a topographic image of the deformations between the A617 driver and 316H column. The average deformation from Sample 2 was lower compared to Sample 1, which experienced more temperature cycles and two room temperature to peak temperature cycles. This test sample is currently in-progress with repeated temperature cycling to assess the strain range performance and to study the influence of the repeated heating and cooling to room temperature.

The induction heating setup could accelerate the test time for the tests shown so far. The WFSTA holder gadget is undergoing fabrication. This gadget will be used to hold a WFSTA during the induction heating setup. The WFSTA sample will be subjected to temperature cycles through an induction heating setup similar to the temperature cycles discussed above. The WFSTA testing through induction heaters will commence in the next fiscal year.

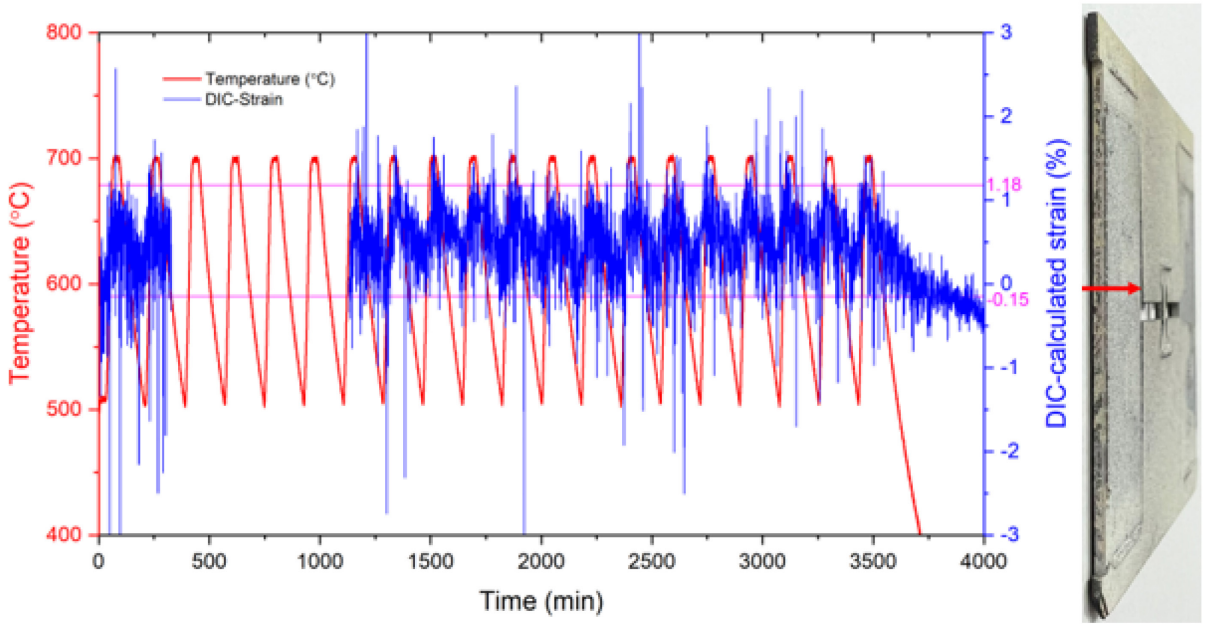

Figure 18. Temperature and DIC-strain on the WFSTA Sample 2 for 20 cycles, and the specimen after cooldown to room temperature with a red arrow showing the out-of-plane deformation of driver-and-specimen assembly.

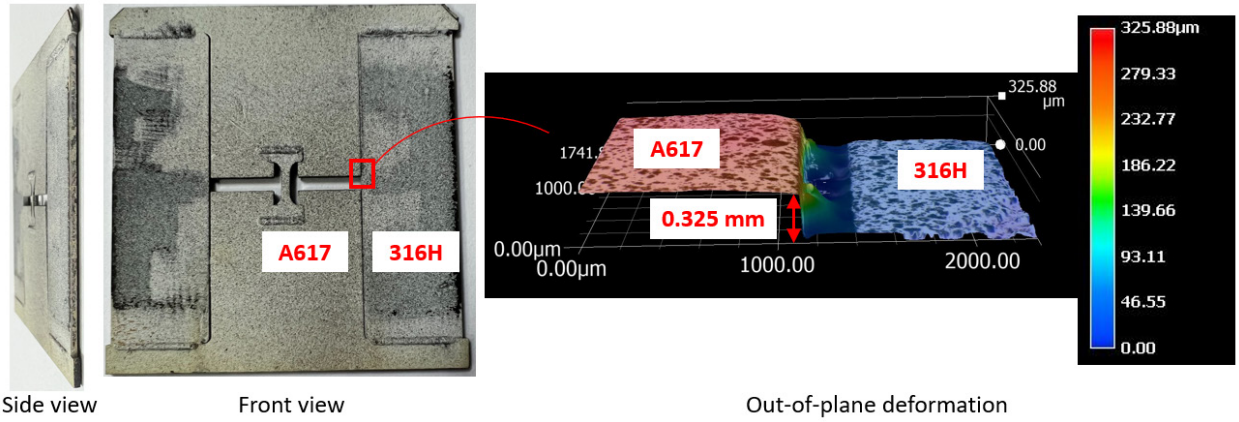

Figure 19. Bent WFSTA Sample 2 with the image showing the out-of-plane deformation at one location between A617 driver and 316H column.

4. INTERLOCKING FLAT SURVEILLANCE TEST ARTICLE

The WFSTA experiments have shown that the test article size could be reduced; however, this is only possible if the driver material has a lower CTE compared to specimen and columns. Refractory alloys have better creep properties and high resistance to corrosion in the molten salt environments compared to stainless steels. This ensures the damage would not affect the driver material performance, providing consistent test data over time. Consider an example with a goal to design flat surveillance test article for the temperature cycle shown in Figure 20. Using driver material of Alloy 617, the test article geometry is 52 × 50 mm. For TZM, the same design parameter yields specimen geometry of 14 × 23.6 mm. Although this feature makes refractory alloys an attractive driver material, welding refractory alloys to stainless steels or any other typical structural material used in high-temperature reactor is not feasible. This demands for a new load transfer mechanism for bi-metal CTE mismatch design. For cylindrical specimens welds could be replaced by threads; however, threaded regions have a stress concentration which could cause inelastic deformation under cyclic loads and is a source of additional compliance in the load train. For flat test article design, threads are not the feasible design option. Thus, an interlocking mechanism is used as a load transfer system. The following subsections present the design approach, fabrication and testing of interlocking flat surveillance test article (IFSTA).

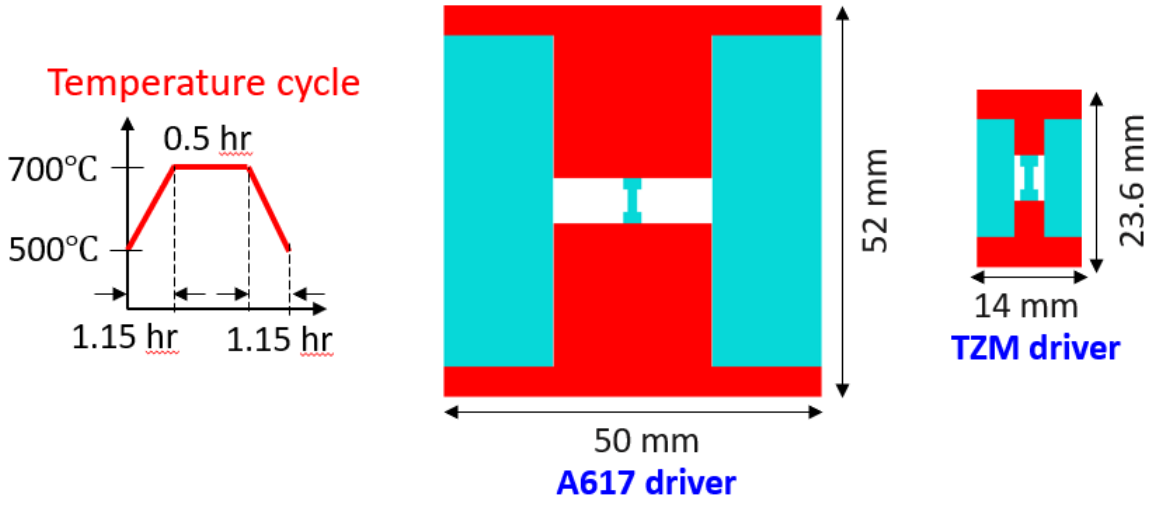

Figure 20. Test article geometry comparison with a given temperature cycle for specimen and column material of 316H shown in blue-colored and red-colored driver material A617 and TZM.

4.1. Design Approach and Test Setup

The design approach uses the same procedure as a flat test article design. First two steps in the design and analysis approach are identical. In the third step, the FE model replaces welds by two contact surfaces. Contact elements are used with normal hard surface and tangential rough properties, capturing interactions between the specimen and driver and between the columns and driver. Unlike welded test articles, the columns and driver material can have a small slack, which could affect the characteristics of the test article. Thus, it is critical to fabricate the column lengths precisely. The first version of specimen geometry, fabricated parts, and test article assembly is shown in Figure 21. In the test article assembly, the red-colored material is TZM, and the rest of the material is Alloy 709. The TZM, highlighted in red color, directly participates in the thermal expansion mismatch and load transfer mechanism. The TZM, which is not highlighted in red color, located on each side of the columns provides support to the column and does not participate in the load-transfer mechanism. A cover plate is bolted on the top and bottom to prevent columns from sliding (blue color) as well as the specimen perpendicular to the specimen axis. (Note that bolts did not transfer any load to the test assembly. Bolts only held the top and bottom plate from sliding.)

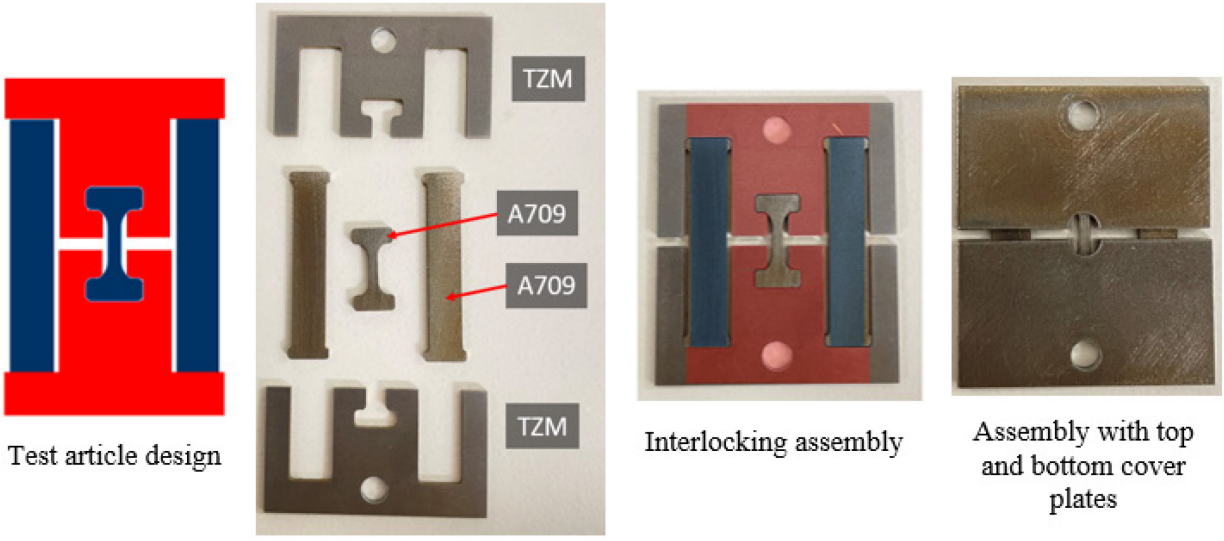

Figure 21. Interlocking test article assembly with TZM and A709.

To avoid the oxidation of TZM in an open-air environment, the entire test sample is enclosed in a glass capsule. The final glass capsule assembly is shown in Figure 22. The front of the capsule, where specimen are located, was made from the plate of optically clear quartz for a DIC. This plate was then fused to the outer cylinder as optically clear quartz cannot be shaped into the bottom of a tube. The total dimensions of the surveillance test article will increase with temperature. Test article corners were chamfered to provide clearance between the specimen and tube to ensure that there is not any free body motion of the test article in the capsule. An inner tube was installed to hold the specimen against the front window. Ceramic wool was installed between the inner tube and the specimen to hold the specimen steady and to accommodate the expansion of the specimen. The capsule is evacuated and 0.25 atmosphere of argon is put back into the capsule before the capsule is sealed. The longer length of the capsule minimizes the heating of the test article during encapsulation process.

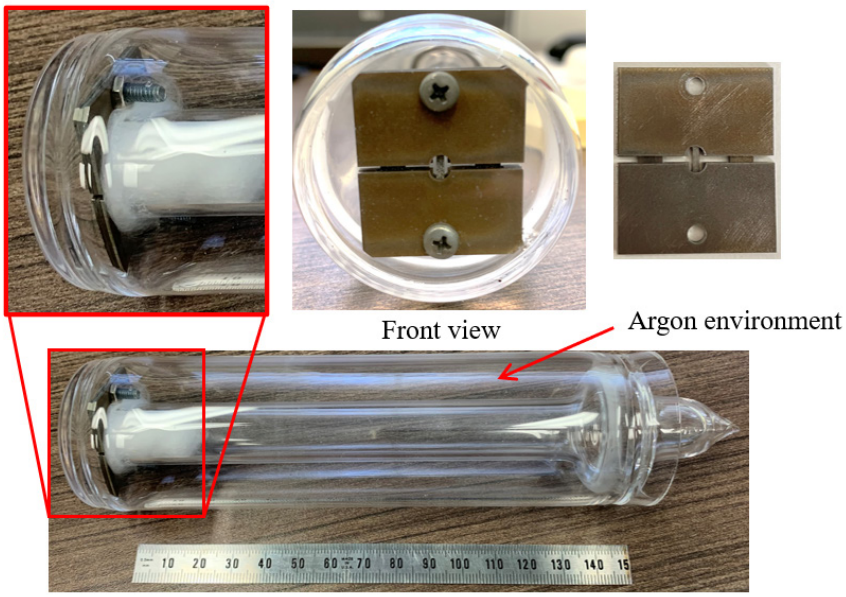

Figure 22. Interlocking test article in glass assembly with argon gas environment. The furnace heating test setup was used to test this test article.

The interlocking test article in a glass assembly is placed in the tube furnace. In the interlocking test article assembly, recording specimen temperature was not feasible. The rest of the test setup was similar to the test setup used for the WFSTA.

4.2. Test Results

Figure 23 shows the DIC-strain during thermal cycling on an IFSTA encapsuled in glass. Images with good speckle patterns were obtained when the temperature was below 700°C (Figure 23b). However, as the temperature increased to 700°C, the speckle pattern was destroyed by the high temperatures (Figure 23c). It should be noted that the speckle pattern was prepared by a spray-painting method not the airbrush method. As a result, the speckle pattern was not able to provide strain data during the experiment. The test article was cooled down to room temperature. Based on the recorded test data, it was concluded that the interlocking mechanism was engaged, and strain accumulation started during the initial temperature ramp. However, strain values and strain range could not be verified due to the speckle pattern's unreliability and lack of data for at least one temperature cycle.

The new IFSTA was repainted with the airbrush method and is currently undergoing temperature cycles. The DIC data will be presented in the next fiscal year.

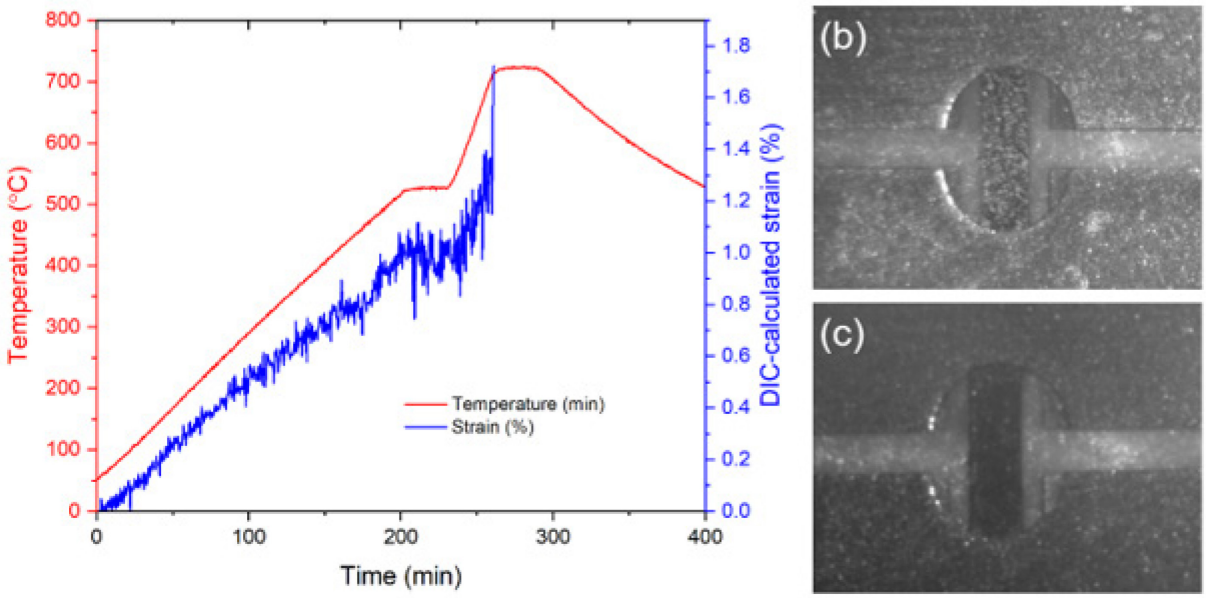

Figure 23. Evolution of DIC-strain during thermal cycling of an IFSTA.

5. SUMMARY AND FUTURE WORK

This report has shown that the flat surveillance test article design with dimensions and volume is a viable design for materials surveillance by more than order of magnitude as compared with the ANL cylindrical design. Two fabrication approaches were identified for the surveillance test article assembly: (1) a welded test article and (2) an interlocking test article.

1. It was shown from thermal cycling (500/700/500°C) in a tube furnace and DIC strain measurements that the version 2 design of the WFSTA can deliver the required strain range. This testing also demonstrated that the design could survive and capture strain ranges of repeated heat-up/cooldown cycles. Some other designs could lead to significant distortion or even failure of the test article during cooldown.
2. The use of the induction heating technique with the "pancake" design showed that the heating and cooling rates in the thermal cycling of the WFSTA can be reduced significantly. The improved "pancake" design shows promise for further optimization to arrive at more uniform temperature distribution in the WFSTA.
3. While the speckle pattern was defective in the initial thermal cycling test of version 1 of the IFSTA in an inert environment, it demonstrated that the interlocking design engaged properly during the heat-up step. The use of an improved speckle pattern to prepare a new IFSTA is in progress. The thermal cycling test of this new test article in a tube furnace is scheduled for FY-24.

Planned work for FY-24 includes the following:

1. Validate the interlocking flat test article design. The refractory metal driver will be replaced by A617 so that thermal cycling can be conducted in the air using the optimized "pancake" design for induction heating to expediate the validation process by removing the complication from air oxidation of refractory metal.
2. Conduct a thermal cycling test of the ANL cylindrical test article until failure, using the furnace heating setup to get the strain history data.

3. Based on the information collected so far on the flat test articles, new and improved flat test article designs will be developed. They will be tested until failure to study the strain evolution history, failure mechanisms, and the performance in the welded regions. These data will be used to support the development of remaining life assessment methodologies.
4. Restart the work on developing acceptance criteria for continued reactor operations. The work was initiated at ANL [11], but the effort was suspended due to programmatic constraint. INL and ANL will collaborate on this development.

6. REFERENCE

[1] ASME Boiler and Pressure Vessel Code. 2023. Section III, Rules for Construction of Nuclear Facility Components, Division 5, High Temperature Reactors. American Society of Mechanical Engineers, New York, NY, USA.

[2] ASME Boiler and Pressure Vessel Code. 2023. Section XI, Rules for Inservice Inspection of Nuclear Reactor Facility Components, Division 2, Requirements for Reliability and Integrity Management (RIM) Programs for Nuclear Reactor Facilities. American Society of Mechanical Engineers, New York, NY, USA.

[3] U.S. Nuclear Regulatory Commission. 2023. "Material Compatibility for Non-Light Water Reactors-Draft Interim Staff Guidance." DANU-ISG-2023-01, ADAMS Accession No.: ML22203A175.

[4] ASME Boiler and Pressure Vessel Code. 2023. Section III, Rules for Construction of Nuclear Facility Components, Division 1, Subsection NB Class 1 Components. American Society of Mechanical Engineers, New York, NY, USA.

[5] ASTM International. Standards E531-13. "Standard Practice for Surveillance Testing of High-Temperature Nuclear Component Materials (Withdrawn 2022)." American Society for Testing and Materials. Last modified January 17, 2022. https://www.astm.org/e0531-13.html .

[6] Wang, Y., T.-L. Sham, and R. I. Jetter. 2015. "Alloy 617 Creep-Fatigue Damage Evaluation Using Specimens with Strain Redistribution." Journal of Pressure Vessel Technology 137 (2): 1–6. https://doi.org/10.1115/1.4028054.

[7] Messner, M. C., et al. 2020. "Initial Development of an In-Situ, Passive Material Surveillance Test Article for Monitoring High Temperature Reactor Structural Components." ANL-ART-198, Argonne National Laboratory. https://doi.org/10.2172/1660408.

[8] Messner, M. C., et al. 2021. "Fabrication and Testing of Two Passively Actuated Creep-Fatigue Surveillance Test Articles." ANL-ART-228, Argonne National Laboratory. https://doi.org/10.2172/1822414.

[9] Messner, M. C., Y. Momozaki, and E. Boron. 2022. "Report on Thermal Cycling Testing and Bimaterial Weld Development for a Passively Actuated Materials Surveillance Test Article." ANL-ART-245, Argonne National Laboratory. https://doi.org/10.2172/1846247.

[10] McMurtrey, M. D., et al. 2022. "Phase II Development of the Surveillance Test Articles to Improve the Design, Fabrication, and Testing." INL/RPT-22-69281, Idaho National Laboratory. https://inldigitallibrary.inl.gov/sites/sti/sti/Sort_63626.pdf.

[11] Messner, M. C. and T.-L Sham. 2021. "Preliminary Procedures and Acceptance Criteria for in-situ Structural Materials Surveillance for MSR." ANL-ART-229, Argonne National Laboratory. https://www.osti.gov/biblio/1817876.

[12] Quino, G., et al. 2020. “Speckle Patterns for DIC In Challenging Scenarios: Rapid Application and Impact Endurance.” Measurement Science and Technology 32 (1): 015203. http://dx.doi.org/10.1088/1361-6501/abaae8.

Appendix A

Digital Image Correlation

In this study, the strain evolution of the test articles was obtained by employing the digital image correlation (DIC) technique. DIC is a non-contact method that enables the measurement of full-field strain, displacement, and deformation of specimen during mechanical and thermal loading. The basic concept of DIC is the correlation of a series of deformed test article images to a reference image that is taken at the deformation-free condition. This principle of DIC requires the sample surfaces to have random patterns with high contrast. As DIC algorithms calculate deformation information based on the input images, the quality of the speckle patterns is very critical. A random speckle pattern is usually required on the test articles to provide high-quality intensity variation that enhances the tracking of points during DIC analysis. As discussed in Quino, et al (2020) [12], there are general requirements for a good speckle pattern: (1) random speckles that ensure recognizable patterns, (2) speckles with appropriate sizes based on the sample size and area of the interested region, (3) a good bond between the speckle pattern and the sample that ensures simultaneous deformation, (4) no cracking of the speckle pattern during deformation before the test ends, and (5) no effects of the patterns on the properties of the materials.

In the present work, speckle patterns were created on the test articles using an airbrush. Airbrush was selected as this spray-painting method to ensure the creation of random fine speckle patterns due to the miniature size of the test articles investigated in this study. The airbrush method is also preferred over other methods that consume more effort such as lithography and focused ion beam (FIB) approaches. To create a high contrast speckle pattern, a white background was applied on the samples by spraying a high-temperature paint. The samples with the white paint were dried at room temperature for more than 12 hours. Subsequently, a high-temperature black paint was applied on the specimen using an airbrush. Once the speckle pattern was applied, the quality of the pattern was inspected using a camera (FLIR Blackfly BFS-U3-27S5M). The DIC analysis software used in this study includes (1) Ncorr, an open-source MATLAB software that enables two dimensional DIC (2D-DIC) analysis, and (2) GOM Correlate, a powerful commercial DIC software from GOM Metrology that allows customized processing of results. In this study, different DIC software was selected for the objective of studying the variation of strain profiles analyzed using different DIC algorithms and to test the capabilities of different DIC software.

These tests were carried out by performing two room-temperature tensile tests (SS316L and Inconel 625) during which the images of the samples were continuously captured. The recorded images were post-processed using Ncorr and GOM Correlate to obtain the strain evolution during the tensile test. The strain profiles obtained by DIC were compared to the extensometer to validate the fidelity of the DIC setup. Subset-based full-field analysis was used for DIC analysis in this study. The key parameters for the subset-based full-field method include subset size, subset shape, and step size. These parameters were determined based on the pixels of the images for different test articles and were mentioned later.

A-1. DIC: Room Temperature Tension Test

Two room-temperature tensile tests were performed on SS316L and Inconel 625. Figure 24 exhibits the experimental setup for room-temperature tensile tests conducted on both SS316L and Inconel 625 flat specimen (ASTM E8/E8M-21). The tensile specimen with speckle patterns were loaded onto an Instron universal testing machine (5980 Series). The FLIR camera was positioned perpendicular to the tensile specimen, which experienced uniaxial tensile loading in the longitudinal direction. In addition to the FLIR camera, the Instron system is equipped with a low-resolution camera (marked as Instron camera in Figure 24) that functions as a virtual extensometer for a deformation measurement. The images taken by the Instron camera were also used for DIC analysis to study the effects of image resolutions on DIC results. Tensile testing was conducted with a constant crosshead rate of 1.0 mm/min. A total of 7% tensile strain was applied on both specimen. The testing stopped once a 7% strain was achieved.

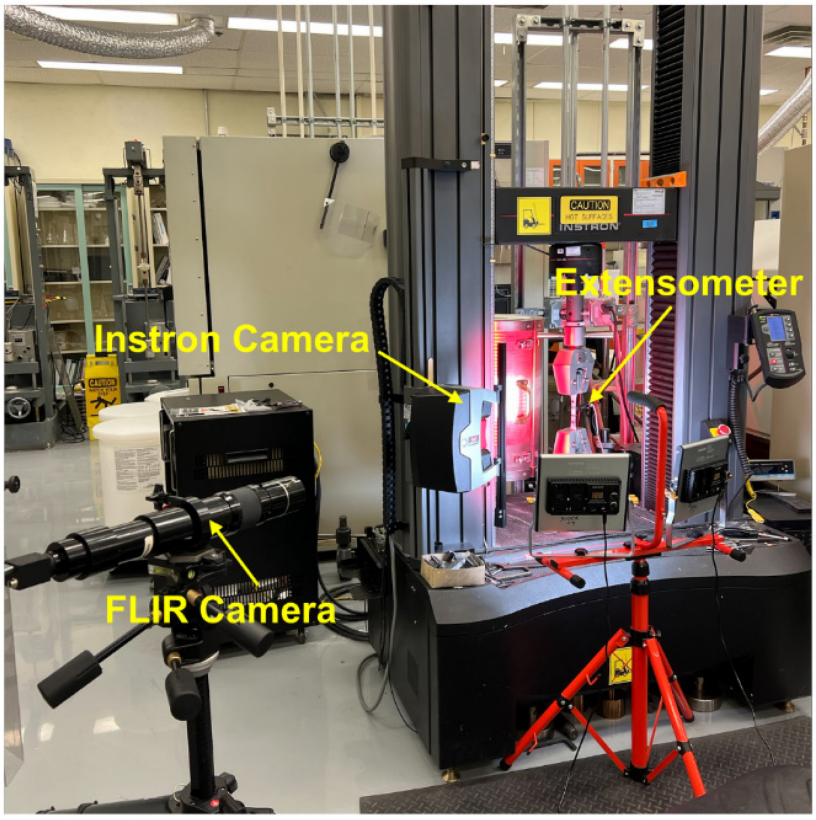

Figure 24. Experimental setup for room-temperature tensile testing on flat tensile specimen.

The images captured by both the Instron camera and FLIR camera during tensile testing were analyzed. A subset size of 5 pixels and subset spacing of 5 pixels were used for DIC analysis for the images taken by the Instron camera due to the image resolution (2048×300 pixels) and field of view. The FLIR camera (1936×1464 pixels) captured images using a subset size of 25 pixels and subset spacing of 15 pixels Figure 25 shows the end-of-test engineering strain of the specimen analyzed by GOM Correlate. The average strain over the investigated area, depicted in Figure 25a, was used to compare the strain measured by the extensometer.

The strain evolution and stress-strain curves for the SS316L specimen measured by DIC and the extensometer are shown in Figure 26a and Figure 26b, respectively. As displayed in Figure 26a, the DIC strain profiles have good agreement with the extensometer at strains lower than 3%. At higher strains, DIC strain tends to increase more sharply compared to the extensometer data. At the end of the test, the strain measured by DIC was 7.71% (Ncorr-Instron camera), 7.68% (Ncorr-FLIR camera), 7.46% (GOM-Instron camera), and 7.57% (GOM-FLIR camera), which demonstrate a 6.57–10.14% increase when compared to the extensometer strain. Such discrepancy might be caused by the accuracy of the extensometer. For the objective of this study, the total strain of ~3% was expected during the thermal cycling of the test articles. Therefore, the DIC strain shows good fidelity as a virtual extensometer for strain analysis. It is also worth noting that the strain calculated using the Ncorr shows good agreement with the strain calculated by GOM, except there is a very limited discrepancy at the end of the test (2.6% discrepancy). Additionally, the DIC analysis conducted on the images obtained by both the Instron and FLIR cameras shows good consistency. The stress-strain curves also indicated limited discrepancy of strains between the DIC and physical extensometer. Similar analysis was repeated on Inconel 625. The evolution of strain and stress-strain curves are shown in Figure 27a and Figure 27b, respectively. Similar to the case of SS316L, the DIC strain for Inconel 625 aligns with the extensometer strain at lower strain values, but there is certain discrepancy between them at higher strains. A good agreement was observed between data from the extensometer and DIC.

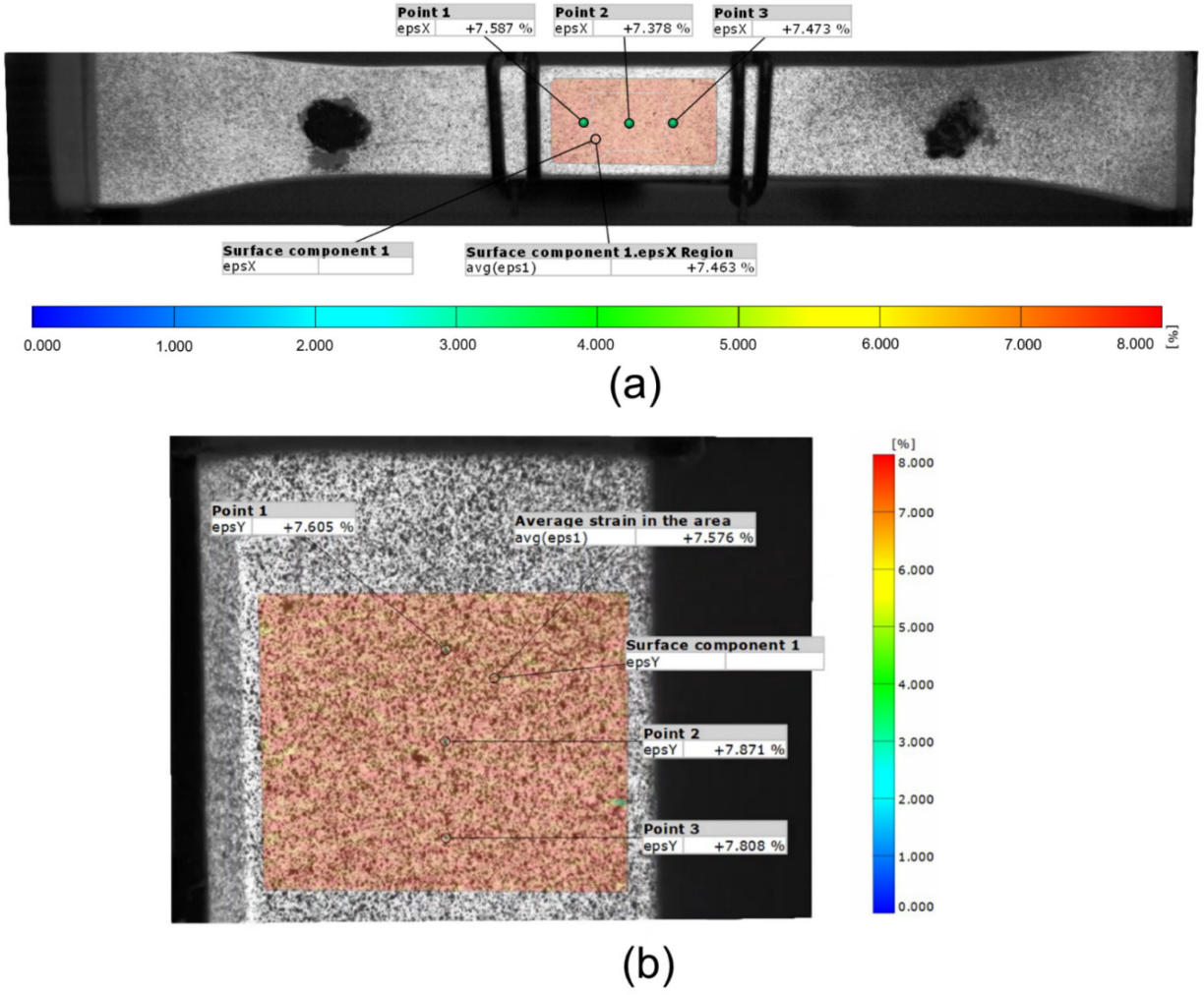

Figure 25. End-of-test engineering strain on SS316L tensile specimen obtained by DIC analysis.

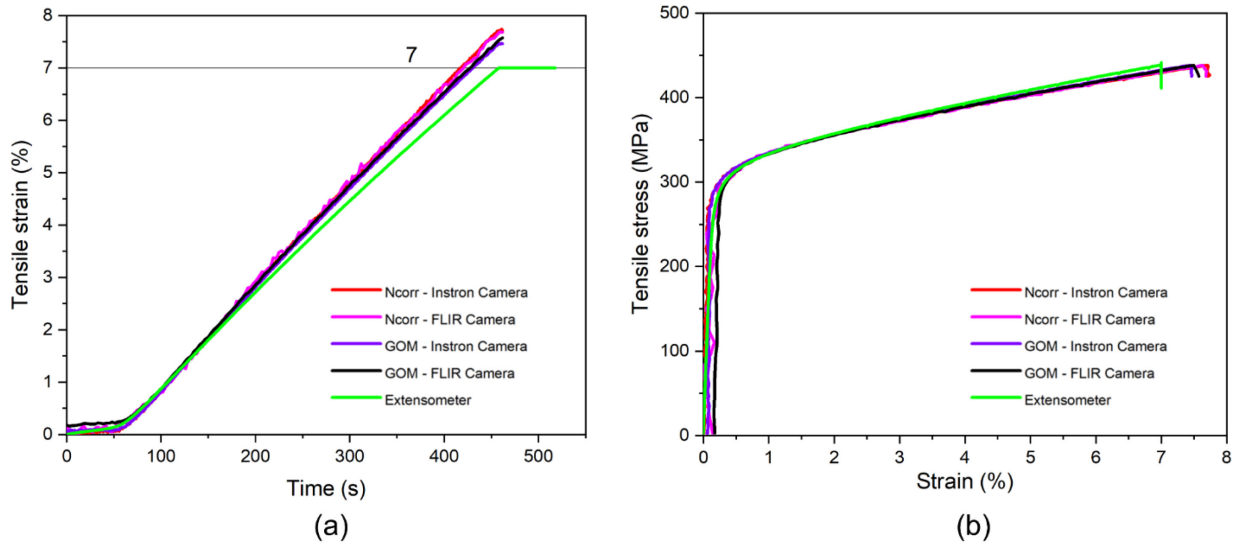

Figure 26. (a) Evolution of DIC strain and extensometer strain and (b) tensile stress-strain curves during tensile testing of SS316L at room temperature.

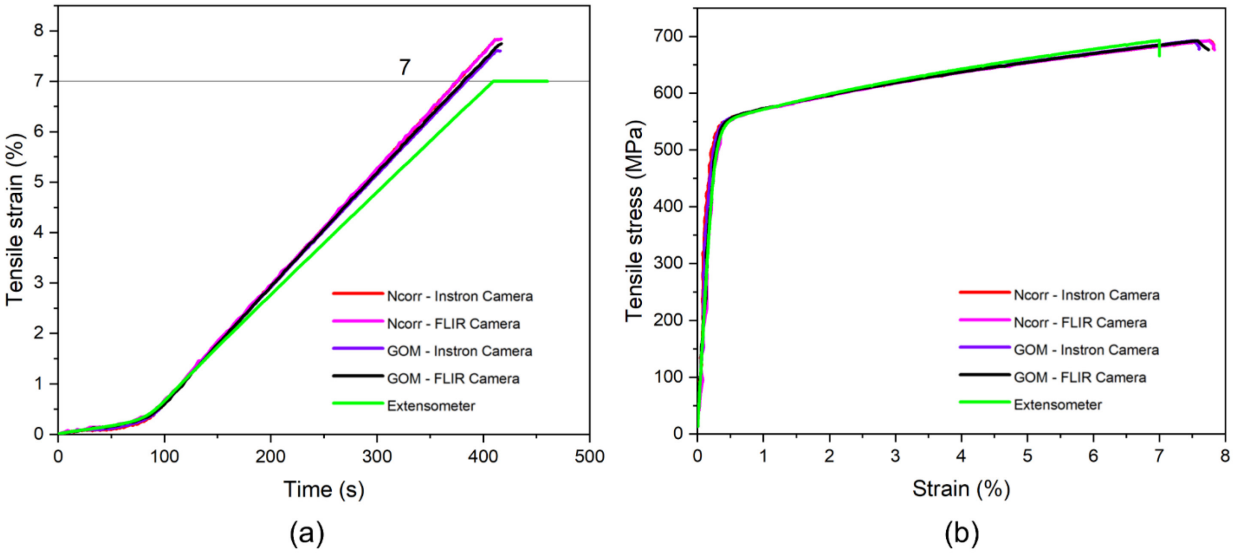

Figure 27. (a) Evolution of DIC strain and extensometer strain and (b) tensile stress-strain curves during tensile testing of Inconel 625 at room temperature.

A-2. DIC: Elevated Temperature Tension Test

Elevated-temperature tensile testing was performed to evaluate the accuracy of the DIC setup compared to the extensometer data. Elevated-temperature tensile testing was conducted using a creep testing frame (Series 2500, Applied Test Systems) with a designed stepped loading due to inaccessibility of a tensile testing system that allows the configuration of both DIC and a physical extensometer. Figure 28a shows the experimental setup. A miniature tensile specimen (SSJ-2) made of SS316L with dimensions shown in Figure 28b was used. The tensile specimen was loaded into the frame. Furnace temperature was raised to 700°C. After soaking the specimen at 700°C for 30 minutes, weights were manually loaded to the specimen following the steps shown in Figure 28c. These steeped loads were calculated to approximately maintain the elevated temperature tension test strain rate. The strain of the sample during testing was measured by an LVDT attached to the top of the loaded plate (after step 1 loading, Figure 28a). Subsequently, the strain was measured by the LVDT until the end of the experiment, while images of the specimen during deformation were continuously taken with an imaging rate of 0.5 Hz. The testing was stopped after a total strain of 16%.

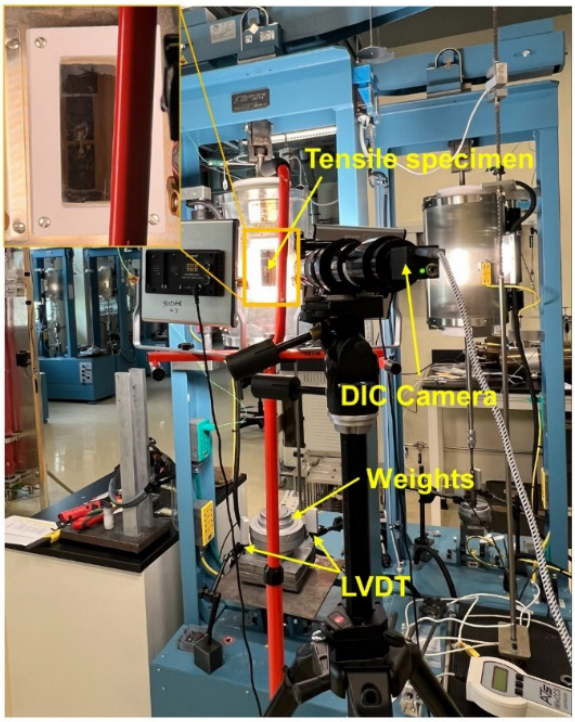

(a)

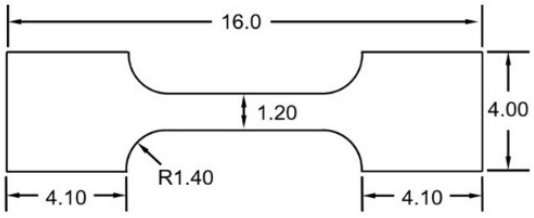

Dimensions in mm, 0.75 mm thickness

(b)

Step	Wait till next load application (s)	Load (lbs)
1	100	20
2	150	3
3	250	5
4	300	7
5	350	7

(c)

Figure 28. (a) Experimental setup for elevated-temperature tensile testing of SS316L in a ATS creep frame, (b) dimensions of tensile specimen, and (c) manual loading procedures.

The captured images were analyzed using GOM Correlate with a subset size of 50 pixels and subset distance of 30 pixels (the dimensions of the images are 1936 × 1464 pixels2). Figure 29a shows the strain at three random points and the average strain over the investigated area. Figure 29b depicts the evolution of strain measured by LVDT and the strain calculated by DIC. It can be seen from Figure 29b that there is good agreement between the LVDT and DIC strains. At the loading steps, a sharp jump of strain occurred, and certain inconsistency was observed between the LVDT and DIC strains. This discrepancy might be caused by sample movement/vibration during the loading process. During the dwell stage, a good match between the LVDT and DIC strains was noted. Such a good match validated the fidelity of the DIC measurement at an elevated temperature of 700°C.

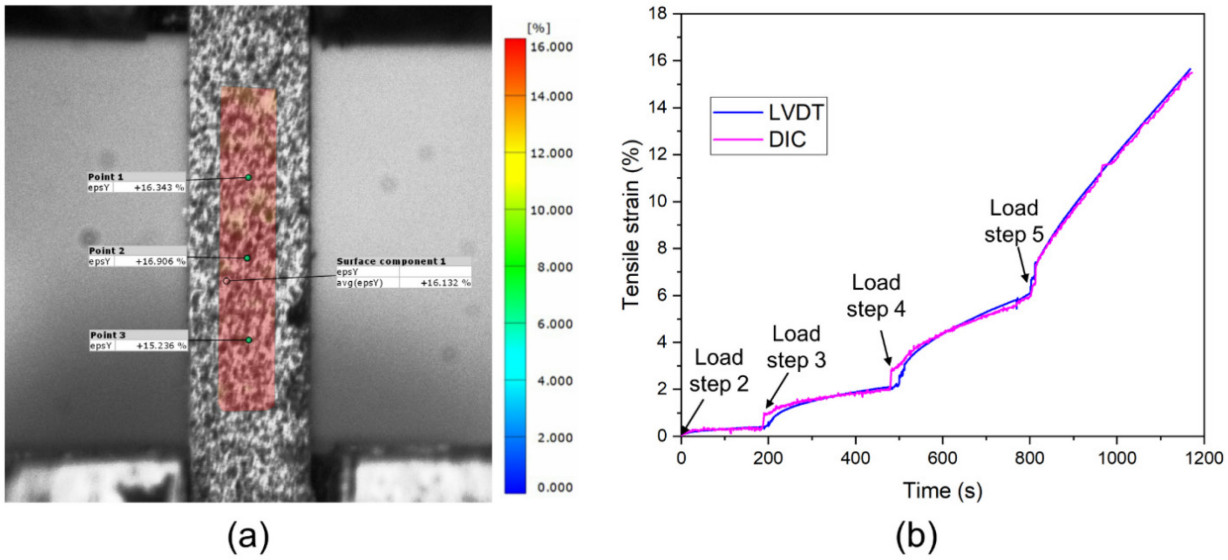

Figure 29. (a) End-of-test strain and (b) strain history obtained by LVDT and DIC in tensile testing of SS316L at 700°C.

A-3. DIC: Short Term Creep Test at Elevated Temperature

The surveillance test articles will experience many cycles of temperature variations to capture material degradations due to a combination of elevated temperature, corrosion, irradiation, fatigue, creep, and creep-fatigue during operation. As a result, the DIC strain under relatively long-term testing beyond tensile test is also critical to validate the DIC results. For this objective, a creep test with DIC was performed in this study. Figure 30a shows the experimental setup for the creep test. The creep test was conducted using an Applied Test Systems (ATS) frame at a temperature of 875°C. A direct loading method was employed. A stress of 30 MPa was applied on a SS316H specimen. Testing continued for 13 hours with an end-of-test creep strain of 0.5%. Figure 30b depicts the strain profiles obtained by LVDT and DIC. A good correlation is observed between the strain from DIC and LVDT. The signal-to-noise ratio in this test was lower compared to the previous tests due to low strain amplitude (<0.5%), which explains the noisy nature of DIC data. Additionally, at 875°C, the images started to saturate due to blackbody radiation at this temperature, which affected the imaging quality. Solutions to address image oversaturation include using blue light and filters. However, good imaging quality was obtained at temperatures from room temperature to 700°C, and therefore, blue light and filters were not pursued for the tasks of this study.

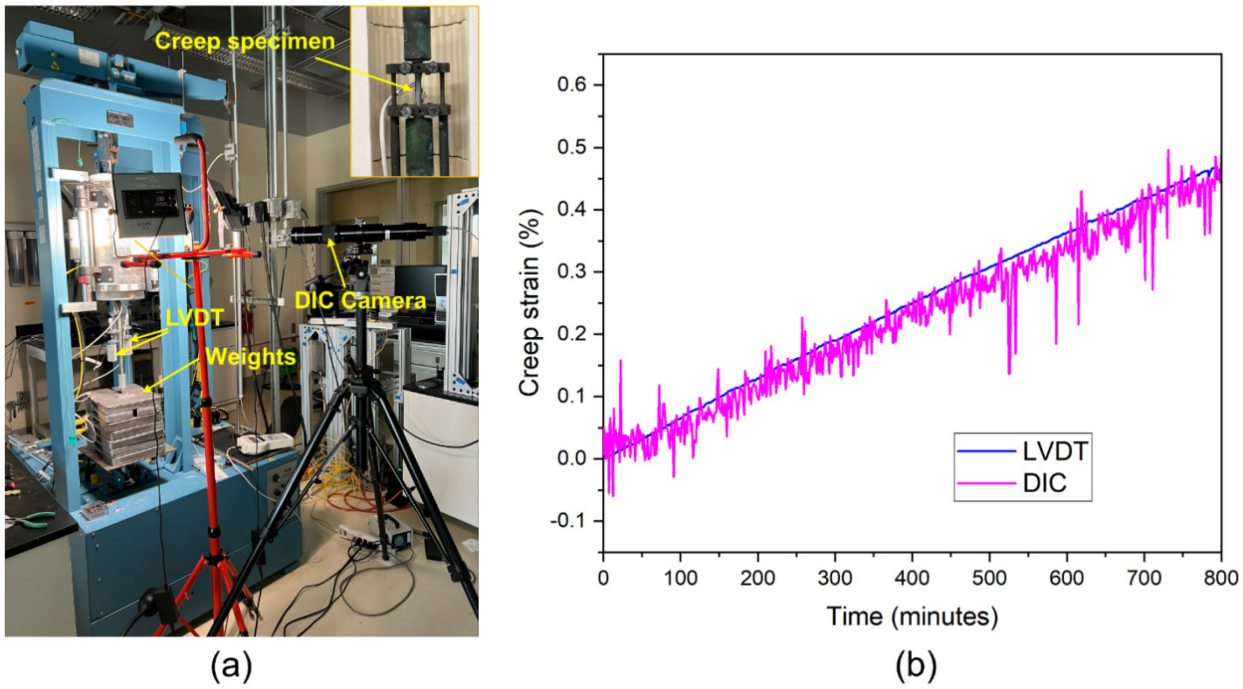

Figure 30. (a) Experimental setup for creep testing of a SS316H specimen at 875°C and 30 MPa, (b) evolution of strain obtained by LVDT and DIC.

These tests validated the speckle pattern technique, DIC test setup, and post-processing software to measure the strain. This setup was selected to be used for the strain measurements of the surveillance test articles.